J. Fluid Mech. (1998), *vol.* 354, *pp.* 239–276. Printed in the United Kingdom

A numerical study of the evolution and structure of a turbulent shear layer under a free surface

By WU-TING TSAI

Department of Oceanography, Taiwan Ocean University, Keelung, 202, Taiwan, ROC

(Received 7 October 1996 and in revised form 28 August 1997)

Results from direct numerical simulations of an unsteady turbulent shear layer with a free surface are presented. The emphasis is on the interaction dynamics of the free surface with the coherent vortices in the underlying turbulent shear flow as well as the resulting free-surface signatures. Instantaneous vortex lines and isosurfaces of enstrophy indicate that coherent horseshoe vortical structures emerge from the random initial vorticity field. These horseshoe vortices impinge, break and reconnect onto the free surface, and then appear as two vortex connections with opposite signs on the surface. The two identified vortical structures correspond to 'splatting' and 'swirling' events, which have been observed in other experiments and simulations of free-surface/turbulence flows. Though free-surface depressions form near the vertical-vorticity centres in the connection processes, only a low correlation ($\approx$ 50% to 60%) is found between the free-surface roughness (vertical deformation) and the connected normal vorticity. On the other hand, the free-surface curvatures and the tangential free-surface vorticities are better correlated ($\approx$ 80% to 90%). The balance of enstrophy and the vorticity transport show that stretching and viscous dissipation along the direction of the vorticity vector dominate the vortex dynamics near the free surface. These two transport mechanisms are found to be responsible for the cancellation of the spanwise vorticity of the horseshoe-vortex heads and the annihilation of the surface-connected normal vorticities.

1. Introduction

The interaction between a free surface and the underlying turbulent flow has recently been the subject of active research. This has mainly been provoked by the increasing use in oceanic and naval research of novel remote-sensing instruments that are sensitive to the microscale motions on or near the ocean surface. Another motivation for such interest is the need to parameterize the air–water scalar exchange rate. The transport of passive scalar, such as gas or heat, across the air–water interface is generally controlled by the resistance within the near-surface turbulence on the ocean side. An improved understanding and the predictive formulation of such turbulent flow are both essential for the specification and development of the near-surface turbulence model.

In the previous studies of the interaction of turbulence with the free surface, the physical systems of the interaction processes can be categorized into the interaction of grid-generated turbulence with a free surface, open-channel flow with a free surface and a turbulent jet beneath a free surface. Examples of these studies include: experiments of interaction between grid-generated turbulence and a free surface by

Brumley & Jirka (1987) and Ölmez & Milgram (1992); numerical simulations of the interaction of a flat (ideal) free surface with initially homogeneous and isotropic turbulence by Perot & Moin (1995) and Walker, Leighton & Garza-Rios (1996); numerical simulations of free-surface channel flows by Leighton *et al.* (1991), Lam & Banerjee (1992), Handler *et al.* (1993), Komori *et al.* (1993), Borue, Orszag & Staroselsky (1995) and Pan & Banerjee (1995); and experiments by Komori, Murakami & Ueda (1989) and Rashidi & Banerjee (1988) among many others (see, for example, the monograph by Nezu & Nakagawa 1993); and experiments of a turbulent jet interacting with a free surface by Swean *et al.* (1989), Anthony & Willmarth (1992), Madnia & Bernal (1993) and Walker, Chen & Willmarth (1995).

From a theoretical perspective, an analysis of the general features of turbulence interacting with a free surface was given by Hunt (1984). Accordingly, for a clean free surface with small deformation, the fluctuating shear stress induced on the surface is also small, and the two-layer model of Hunt & Graham (1978) for the interaction between a shear-free boundary and the turbulence is applicable. The theoretical model decomposes the interaction process into a surface-influenced inviscid source layer with thickness roughly the integral length scale of the free-stream turbulence and a thin viscous layer next to the free surface. Within the source layer, the irrotational motions around the impinging turbulent eddies are distorted by the free surface, and the turbulent energy is redistributed from the vertical to the horizontal components of the velocity. The viscous effect is confined within a thin sublayer of thickness $O(\ell_e Re_e^{-1/2})$, where Re_e is the Reynolds number based on the impinging eddy velocity u_e and the length scale ℓ_e. A small reduction in the horizontal velocity of $O(u_e Re_e^{-1/2})$ is caused within this sublayer, and the rate of attenuation of the vertical velocity is increased by $O(Re_e^{-1/2})$.

In this work, as a canonical problem, the interactions among a free surface, a mean shear flow and initially isotropic three-dimensional turbulent fluctuations are studied by the direct numerical simulation of the flow. The physical process of the canonical problem corresponds to a turbulent shear current beneath the air–water interface where the mechanism that generates the shear layer, such as wind stress, is no longer operative. Shear flow in the near region beneath the ocean surface can be decomposed into wind- and wave-induced components (Wu 1975), and it consists mainly of the wind-induced current at short fetches and of the wave-induced transport at long fetches (Wu 1983). The former component of a shear layer, the free-surface deformation of which is mild, is of particular interest in the present study. For large-amplitude free-surface flows, breaking waves occur naturally, and the turbulence is generated by surface breaking and the bubbles that may be produced. At the present time, the development of a direct numerical simulation method for such an oceanic flow is somewhat unrefined. For most of the calculations of free-surface/turbulence flows to date, only the case of zero Froude number (free-slip flat surface) (e.g. Leighton *et al.* 1991; Lam & Banerjee 1992; Perot & Moin 1995; Pan & Banerjee 1995; Walker *et al.* 1996) and weakly nonlinear approximations of the free-surface boundary conditions (Borue *et al.* 1995) have been considered. The only fully nonlinear calculation of free-surface/turbulence flow is that of Komori *et al.* (1993) although, in that study, only flows with small free-surface deformation were simulated. In the present study, the effect of free-surface deformation is included through weakly nonlinear approximations of the free-surface boundary conditions as in Borue *et al.* (1995).

For turbulent shear flows, such as a turbulent boundary layer, organized vortical structures in the vorticity field have previously been identified in both experiments

and numerical simulations (see, for example, the review by Robinson 1991). It is not surprising, therefore, that coherent vortices also arise from the turbulent shear flow underneath the free surface and that they interact with the surface. Though this issue has been addressed in some previous studies on the interaction of turbulence with a free surface (e.g. Komori *et al.* 1989; Pan & Banerjee 1995), there has been very little discussion of the detailed correlations between the surface signatures and the underlying coherent vortical structures. For a free surface without contamination or external shear stress, a normal connection of the vortex to the surface can be explained by the kinematic conditions of vorticity on the free surface. However, even the processes by which a vortex breaks and reconnects its ends to the free surface in a laminar flow have been subject of many debates (Gharib 1994) and active research (e.g. Gharib & Weigand 1996). In addition, the correlations between the free-surface signatures and the connected and subsurface (unconnected) vortical structures have been very little discussed. Hence, it is the objective of the present numerical study to provide a better understanding of the interaction dynamics as well as the correlated surface features in the interaction processes.

The paper is organized as follows. The mathematical formulation of the physical process and the detailed numerical aspects of the simulation are presented in §2 and §3 respectively. To elucidate the blocking effect of the free surface, the balance of turbulence energy and the length scales of turbulence near the free surface are discussed in §4.1 and §4.2, respectively. The vertical distribution of the vorticity field near the free surface is addressed in §4.3. Organized free-surface signatures arising from the interaction of the underlying vortical flow with the free surface are presented in §4.4. The possible correlations between the free-surface roughness and the vorticity field are also discussed. The underlying horseshoe and surface-connected coherent vortical structures are identified and confirmed in §4.5. The connecting processes of the coherent vortices with the free surface are then considered in §4.6. Finally, in §4.7, by examining the enstrophy balance and the vorticity transport, it is shown that the dominant vortex dynamics near the free surface can be attributed to the interaction of the coherent vortices with the free surface.

2. Mathematical formulation

The motion of a three-dimensional viscous incompressible bulk flow as well as the free surface are considered here. The coordinate axes $x_i = (x_1, x_2, x_3)$, moving with the initial free-stream velocity U_0 of the shear layer, are in the streamwise, spanwise and vertical directions, with the corresponding velocities $u_i = (u_1, u_2, u_3)$. All flow variables are non-dimensionalized by the characteristic depth of the initial shear layer D_0, the free-stream velocity U_0 and the density of the bulk fluid ρ. In the context of a Newtonian incompressible bulk fluid, conservation of mass and momentum specify that

$$u_{i,i} = 0, \tag{2.1}$$

and

$$u_{i,t} + u_j u_{i,j} + p_{,i} - \frac{1}{Re} u_{i,jj} = 0, \tag{2.2}$$

where p is the dynamic pressure, $Re = U_0 D_0 / \nu$ is the Reynolds number, and ν is the kinematic viscosity of the bulk fluid. The Einstein summation convention has been adopted, and a comma denotes differentiation.

The physical conditions that there be no mass flux and conservation of linear

momentum across the free surface $x_3 = \eta(x_1, x_2, t)$ give rise to the kinematic condition and the dynamic conditions for the stress field on the free surface. Based on the analyses of Tsai & Yue (1995) (see also Borue *et al.* 1995), the free-surface boundary conditions are linearized by assuming a free-surface deformation of the order of $\epsilon \sim O(Fr^2)$ and a free-surface boundary layer of thickness $\delta \sim O(Re^{-1/2})$, with $\delta^2 \ll \epsilon \ll \delta \ll 1$. Carrying out the perturbation expansion about the mean free surface $x_3 = 0$, the kinematic condition up to $O(\epsilon)$ is

$$\eta_{,t} + (u_1\eta)_{,1} + (u_2\eta)_{,2} - u_3 = 0, \tag{2.3}$$

the normal-stress condition up to $O(\epsilon)$ is

$$-p + \frac{\eta}{Fr^2} + \frac{2}{Re}u_{3,3} = \frac{1}{We}(\eta_{,11} + \eta_{,22}), \tag{2.4}$$

and the tangential-stress conditions in the x_1- and x_2-directions up to $O(\delta)$ are

$$u_{1,3} + \eta u_{1,33} + u_{3,1} = 0, \tag{2.5}$$

$$u_{2,3} + \eta u_{2,33} + u_{3,2} = 0. \tag{2.6}$$

The non-dimensional parameters in the boundary conditions are the Froude number $Fr = U_0/(gD_0)^{1/2}$ and the Weber number $We = \rho U_0^2 D_0/\sigma_0$, where g is the gravitational acceleration and σ_0 is the surface tension. The weakly nonlinear free-surface conditions considered in the present study correspond to those physical processes where the turbulence energy is larger than the wave energy. A direct numerical simulation of the large-amplitude free-surface motions interacting with fully developed turbulence is somewhat premature at this point. The present formulation of the problem, although only considering weakly nonlinear interactions among waves while retaining fully nonlinear interactions of the turbulence, is totally consistent and sufficient to capture the interaction dynamics between the free surface and the underlying turbulence – the main objective of the present study.

To derive the equation governing the energy conservation, the material time derivative of the kinetic energy of the flow integrated over the fluid volume V ($\equiv \mathrm{d}E_k(t)/\mathrm{d}t$) is given by

$$\frac{\mathrm{D}}{\mathrm{D}t}\int_V (\tfrac{1}{2}u_i u_i)\mathrm{d}V = -\int_V (u_i p)_{,i}\mathrm{d}V + \frac{1}{Re}\int_V [u_i(u_{i,j} + u_{j,i})]_{,j}\mathrm{d}V - \frac{1}{Re}\int_V u_{i,j}(u_{i,j} + u_{j,i})\mathrm{d}V. \tag{2.7}$$

Using the divergence theorem in conjunction with the free-surface boundary conditions (2.3) to (2.6), the first and the second integrals can be simplified, and the equation for the conservation of energy up to $O(\epsilon)$ becomes

$$\frac{\mathrm{D}}{\mathrm{D}t}\int_V (\tfrac{1}{2}u_i u_i)\mathrm{d}V = -\frac{1}{2Fr^2}\frac{\partial}{\partial t}\int_{S_0}\eta^2\mathrm{d}S - \frac{1}{We}\int_{S_0}\eta_{,t}(\eta_{,11} + \eta_{,22})\mathrm{d}S - \frac{1}{Re}\int_V u_{i,j}(u_{i,j} + u_{j,i})\mathrm{d}V, \tag{2.8}$$

where S_0 is the mean free surface, $x_3 = 0$. The first term on the right-hand side of (2.8) ($\equiv \mathrm{d}E_\eta/\mathrm{d}t$) represents the rate of change of the potential energy due to free-surface motions. The second term ($\equiv \mathrm{d}E_\sigma/\mathrm{d}t$) stands for the work done by the surface tension. The last term ($\equiv \mathrm{d}E_v/\mathrm{d}t$) represents the rate of energy dissipation caused by viscous stresses. It should be pointed out that the equation of energy conservation

(2.8), albeit a weakly nonlinear form of the fully nonlinear equations of motion, is the exact energy equation for the equation of motion (2.2) and the boundary conditions (2.3) to (2.6) and, as such, should be satisfied in the numerical computation.

3. Numerical simulation

3.1. *Numerical method*

The three-dimensional continuity equation (2.1) and the Navier–Stokes equation (2.2) subject to the weakly nonlinear free-surface boundary conditions (2.3) to (2.6) are solved numerically in a computational domain closed by imposing periodic conditions in both the streamwise and spanwise directions, and by the mean free surface ($x_3 = 0$) and a free-slip boundary on the bottom ($x_3 = -L_3$). The flow variables u_1, u_2 and p are arranged on the discrete grid system, while u_3 is on the vertically staggered grids. Both the continuity and Navier–Stokes equations are satisfied on the discrete grids with u_1, u_2 and p arranged on them. The spatial-differential operators with respect to x_1 and x_2 are approximated by the pseudo-spectra method, and the operators with respect to x_3 are approximated by the second-order finite-difference scheme.

A low-storage second-order Runge–Kutta method is used for time integrating the Navier–Stokes equation (2.2) for u_i and the kinematic free-surface condition (2.3) for η. Continuity is ensured with the solution being a pressure Poisson equation satisfied on the discrete grids. The pressure Poisson equation is obtained by taking the divergence of the Navier–Stokes equation. The free-slip bottom gives rise to the homogeneous Neumann condition of pressure for the Poisson equation. The normal-stress free-surface condition (2.4) is used as a Dirichlet condition for pressure. An additional solvability condition of the pressure Poisson equation, which is required for the formulations with only the Neumann boundary conditions, is not needed in the present formulation. The pressure Poisson equation is solved at each interval step in the Runge–Kutta time integration.

The tangential-stress conditions (2.5) and (2.6) are satisfied implicitly in integrating the Navier–Stokes equation. To evaluate the convection terms $u_3 u_{i,3}$ and the dissipation terms $u_{i,33}$ in the $i = 1, 2$ Navier–Stokes equation at $x_3 = 0$, the tangential-stress conditions are used to extrapolate the velocities on the artificial grid above the mean free surface. In order to maintain the second-order accuracy of the spatial approximation, these terms are approximated by

$$\left.\frac{\delta(u_3 u_i)}{\delta x_3}\right|_{x_3=0} \equiv \mathscr{D}_c u_i$$
$$= -\frac{1}{24\Delta}\left(23u_3|_{1/2}u_i|_{1/2} - 21u_3|_{-1/2}u_i|_{-1/2} - 3u_3|_{-2/3}u_i|_{-2/3} + u_3|_{-5/2}u_i|_{-5/2}\right), \quad (3.1)$$

and

$$\frac{1}{Re}\left.\frac{\delta^2 u_i}{\delta x_3^2}\right|_{x_3=0} \equiv \mathscr{D}_d u_i = \frac{1}{Re}\frac{1}{12\Delta^2}\left(11u_i|_1 - 20u_i|_0 + 6u_i|_{-1} + 4u_i|_{-2} - u_i|_{-3}\right), \quad (3.2)$$

where $u_i|_q$ $(i = 1, 2)$ represents velocity u_i at $x_3 = q\Delta$, and Δ is the vertical discretization. The velocities on the artificial grids above the free surface are evaluated by

$$u_i|_1 = 3\Delta[u_{i,3}]_{x_3=0} - \tfrac{3}{2}u_i|_0 + 3u_i|_{-1} - \tfrac{1}{2}u_i|_{-2}, \quad (3.3)$$

and

$$u_3|_{1/2} = \tfrac{24}{23}\Delta[u_{i,3}]_{x_3=0} + \tfrac{21}{23}u_3|_{-1/2} + \tfrac{3}{23}u_3|_{-3/2} - \tfrac{1}{23}u_3|_{-5/2}, \quad (3.4)$$

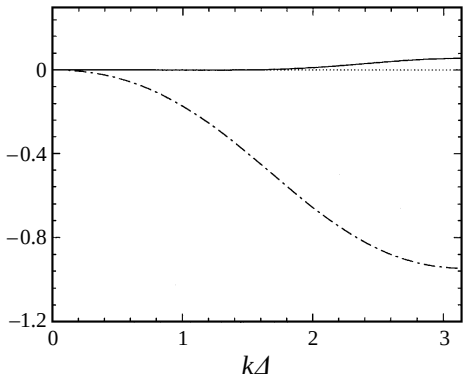

FIGURE 1. Real parts of the eigenvalues λ_c (———) and λ_d (— · — · —) of the operators $\mathscr{D}_c$ and $\mathscr{D}_d$ as functions of non-dimensional grid size $k\Delta$.

where $[u_{i,3}]_{x_3=0}, i = 1,2$ is obtained from the tangential-stress conditions (2.5) and (2.6), and $[u_{3,3}]_{x_3=0}$ from the continuity equation (2.1). The horizontal velocities on the staggered grids near the free surface are evaluated by

$$u_i|_{1/2} = \tfrac{1}{16}\left(5u_i|_1 + 15u_i|_0 - 5u_i|_{-1} + u_i|_{-2}\right), \tag{3.5}$$

and

$$u_i|_{-k/2} = \tfrac{1}{48}\left(-3u_i|_k + 27u_i|_{k-1} - 5u_i|_{k-2} + u_i|_{k-3}\right), \tag{3.6}$$

where $i = 1,2$, $k = 1,3$ and 5.

It has been shown that the improper implementation of the tangential-stress conditions may lead to numerical instabilities and ruin the computation (Tsai & Yue 1996). The linear stability analysis of $u_i(x_3,t) = \sum_k \hat{u}_i(k,t)\mathrm{e}^{\mathrm{i}kx_3}$ for the operators $\mathscr{D}_c$ and $\mathscr{D}_d$ yields $\mathrm{d}\hat{u}_i(k,t)/\mathrm{d}t = \lambda\hat{u}_i(k,t)$, where λ is the complex eigenvalue of the operator. The numerical dissipation of the operator is positive when $\mathrm{Re}\,(\lambda) < 0$. The real parts of the eigenvalues λ_c and λ_d of the operators $\mathscr{D}_c$ and $\mathscr{D}_d$, respectively:

$$\mathrm{Re}\,(\lambda_c) = -\frac{u_3|_0}{1152\Delta}(-135 + 228\cos k\Delta - 126\cos 2k\Delta + 36\cos 3k\Delta - 3\cos 4k\Delta), \tag{3.7}$$

and

$$\mathrm{Re}\,(\lambda_d) = \frac{1}{Re}\frac{1}{24\Delta^2}(-73 + 78\cos k\Delta - 3\cos 2k\Delta - 2\cos 3k\Delta), \tag{3.8}$$

as functions of $k\Delta$ are shown in figure 1, where $\Delta \approx 0.08$, $Re = 1000$, $u_3|_0 \approx 0.01$ in a typical simulation of the turbulence in this study. The artificial dissipation induced by the convection operator $\mathscr{D}_c$ remains negligible in the low-to-intermediate wavenumber range. For high wavenumbers, however, it amplifies the short waves when $u_3|_0 > 0$ (dissipates when $u_3|_0 < 0$). Nevertheless, these amplified high-wavenumber modes (when $u_3|_0 > 0$) are effectively damped by the physical dissipation of $\mathscr{D}_d u_i$, which is positive for the whole range of wavenumbers.

3.2. *Initial condition*

The initial free surface is assumed to be flat. The initial sheared turbulence field is given by adding a three-dimensional fluctuating velocity field to a two-dimensional shear flow: $u_1(x_3) = 1 + (u_c - 1)\ \mathrm{sech}^2(k_0 x_3)$ (Mattingly & Criminale 1972). The values of the profile parameters used are $u_c = 0.0012$ and $k_0 = 0.88137$, such that $(1-u_1)/(1-u_c) = 0.5$ at $x_3 = -1$. The inviscid linear stability analysis of such a shear

layer in the presence of a free surface is also given by Triantafyllou & Dimas (1989). In the present simulation, however, unstable modes are not superimposed onto the mean flow to trigger an unstable evolution.

To ensure the solenoidal property, the initial fluctuating velocity field is expressed in terms of vector streamfunctions. A three-dimensional vector field $\boldsymbol{A}_0(x_1, x_2, x_3)$ with random magnitudes of the components is first generated. The Fourier amplitudes $\hat{\boldsymbol{A}}_0(k_1, k_2, k_3)$ are redistributed according to a Gaussian filtering function:

$$\hat{\boldsymbol{A}}_1(k_1, k_2, k_3) = \hat{\boldsymbol{A}}_0(k_1, k_2, k_3) \exp(-k_j^2/\bar{k}_j^2), \tag{3.9}$$

where $\bar{k}_j$ is the cutoff wavenumber. The filtered vector field $\boldsymbol{A}_1$ is then multiplied by a vertical variation function $f(x_3) = \tanh^4 x_3/\cosh^3 x_3$:

$$\boldsymbol{A}(x_1, x_2, x_3) = f(x_3)\boldsymbol{A}_1(x_1, x_2, x_3). \tag{3.10}$$

The variation function $f(x_3)$ is chosen such that the initial turbulent fluctuating intensities attenuate to very small values near the free surface to ensure that, initially, there are no prescribed flow structures (see figure 11). The variation of the turbulence intensity is roughly equal to the vertical gradient of the mean shear velocity, except in the region near the free surface. With the curl of the vector field $\boldsymbol{A}(x_1, x_2, x_3)$ taken, the resulting velocity field satisfies the requirement of the solenoidal condition. The initial random fluctuating velocity field is then obtained by rescaling the magnitudes of the velocities such that the maximal horizontal-averaging turbulence velocity is u_0' (a given value).

3.3. *Numerical and flow parameters*

The normalized length, width and depth of the computational domain are 10.472, 10.472 and 4, respectively, with periodic conditions in the streamwise (x_1) and spanwise (x_2) directions. The chosen length of the computational domain is around the wavelength (wavenumber = 0.4) of the most unstable mode from the inviscid linear stability analysis. The simulations are carried out with 128^3 grid points. The time step of the Runge–Kutta integration is 0.005. The cutoff wavenumbers for generating the initial fluctuating velocity are $\bar{k}_1 = \bar{k}_2 = 36\pi/10.472$ and $\bar{k}_3 = 7\pi/2$, while the initial maximal horizontal-averaging turbulence velocity is $u_0' = 0.15$. Based on the characteristic depth of the shear layer and the free-stream velocity, the parameters of the flow in the simulation are the Reynolds number $Re = 1000$, the Froude number $Fr = 0.707$ and the Weber number $We = 20$. The chosen Froude and Weber numbers correspond to a flow with $\sigma_0 \approx 73$ g s^{-2}, $D_0 \approx 3$ cm and $U_0 \approx 25$ cm s^{-1}.

Since the turbulence is homogeneous in the horizontal plane, the turbulent fluctuating velocity is defined here as

$$u_i' = u_i - \langle u_i \rangle, \tag{3.11}$$

where $\langle \cdot \rangle$ represents the averaging in the horizontal plane. The Taylor microscales $\lambda_{ij;\alpha}$ are defined as

$$\lambda_{ij;\alpha}(x_3) = \left[\frac{\langle (u_i')^2 \rangle}{\langle (u_{j,\alpha}')^2 \rangle} \right]^{1/2}. \tag{3.12}$$

For the Reynolds number simulated, based on the maximal turbulent velocity $q \equiv \langle u_i' u_i' \rangle^{1/2} \approx 0.1$ and the corresponding Taylor microscale $\lambda \equiv \frac{1}{3}\lambda_{ii;1} \approx 0.6$, the Taylor microscale Reynolds number $Re_\lambda \equiv q\lambda/\nu$ at the end of the simulation ($t = 60$) is about 60.

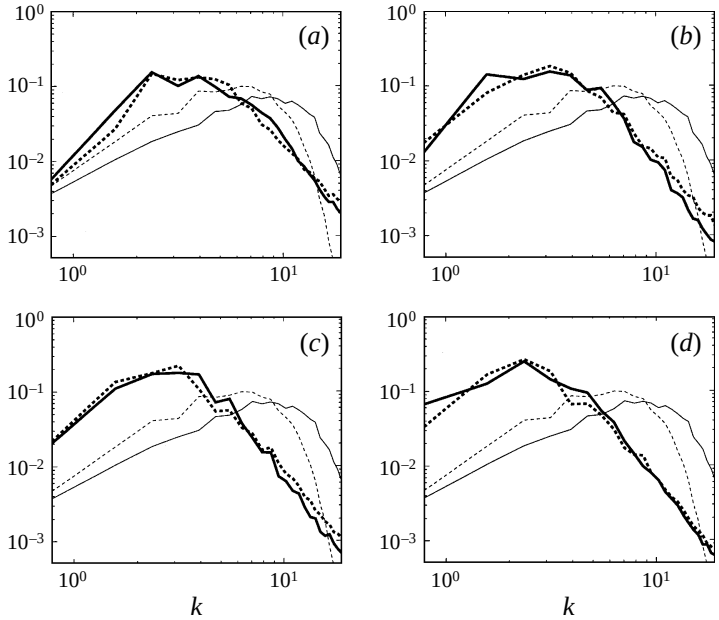

FIGURE 2. One-dimensional energy spectra at $x_3 \approx -0.813$ with initial cutoff wavenumbers $\bar{k}_1 = \bar{k}_2 = 36\pi/10.472$, $\bar{k}_3 = 7\pi/2$ and initial maximal turbulence velocity $u_0' = 0.2$ (- - - - -), and $\bar{k}_1 = \bar{k}_2 = 26\pi/10.472$, $\bar{k}_3 = 5\pi/2$ and $u_0' = 0.15$ (———) for $t = 10$ (*a*), 20 (*b*), 30 (*c*) and 40 (*d*). For comparison, the initial spectra ($t = 0$; thin curves) are shown with the evolved spectra (thick curves).

The Kolmogorov microscale, $\eta_k \equiv (\nu^3/\varepsilon_k)^{1/4}$, at $t = 60$ is approximately 0.082, based on the kinetic-energy dissipation rate of $\varepsilon_k = -\mathrm{d}E_k/\mathrm{d}t \approx 0.218$. The horizontal and vertical grid resolutions are 0.083 and 0.032, respectively. This means that the turbulence in the bulk and near the free surface is well resolved.

3.4. *Validation of the simulation*

Since the initial turbulent velocity field is artificially imposed with only the solenoidal condition being satisfied, it is necessary to determine whether there are any artifacts of the initial conditions which persist as the flow evolves. This is verified through experimentation with the calculations using different parameters in initializing the flow, such as the cutoff wavenumber $\bar{k}_j$ in (3.9), the vertical variation function $f(x_3)$ in (3.10), the maximal initial horizontal-averaging turbulence velocity u_0' and the random vector field. Examples of such numerical experiments showing the evolution ($t = 10$, 20, 30 and 40) of the normalized energy spectra $\mathscr{E}(k, x_3)$ at various depths with different parameters ($\bar{k}_1 = \bar{k}_2 = 36\pi/10.472$, $\bar{k}_3 = 7\pi/2$, $u_0' = 0.15$ and $\bar{k}_1 = \bar{k}_2 = 26\pi/10.472$, $\bar{k}_3 = 5\pi/2$, $u_0' = 0.2$) in the initial fluctuating field are shown in figures 2–4. The one-dimensional energy spectrum on a horizontal plane, $\mathscr{E}(k, x_3)$, is evaluated by integrating the spectrum tensor $e_{ii}(k_1, k_2, x_3)$ over the annuli in the (k_1, k_2)-plane,

$$\mathscr{E}(k, x_3) = \frac{1}{2} \int e_{ii}(k_1, k_2, x_3) \mathrm{d}s(k), \tag{3.13}$$

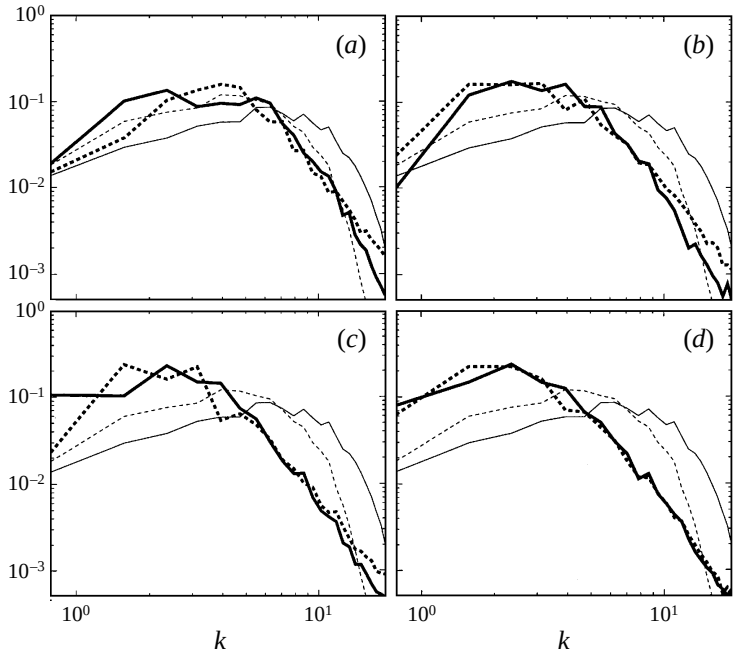

FIGURE 3. Same as figure 2, but at $x_3 \approx -0.188$.

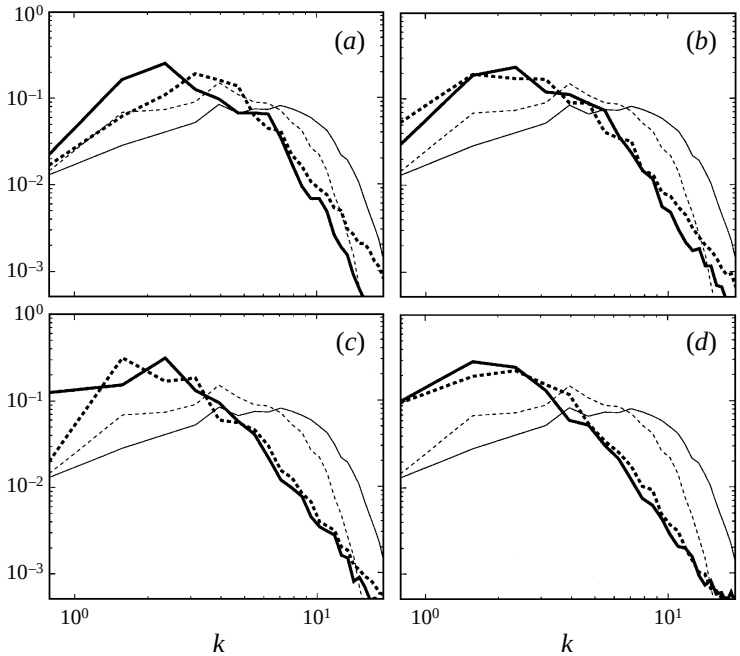

FIGURE 4. Same as figure 2, but at $x_3 \approx -0.031$.

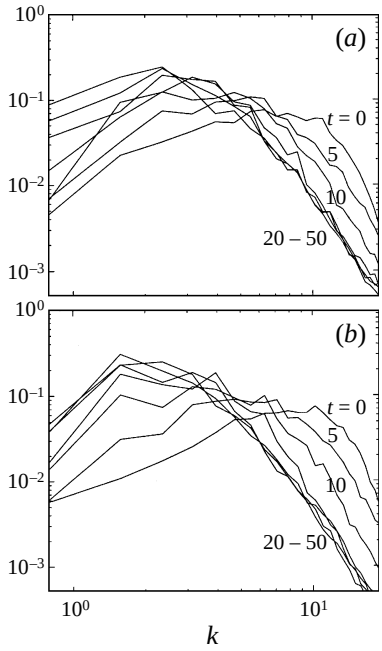

FIGURE 5. Evolution of the one-dimensional turbulent-energy spectra at $x_3 \approx -0.344$ (*a*) and -1.906 (*b*).

where $k^2 = k_1^2 + k_2^2$ is the magnitude of the horizontal wavenumber vector k_α, the spectrum tensor,

$$e_{ij}(k_1, k_2, x_3) = \frac{1}{4\pi^2} \iint R_{ij}(r_1, r_2, x_3) \mathrm{e}^{-\mathrm{i}(k_1 r_1 + k_2 r_2)} \mathrm{d}r_1 \mathrm{d}r_2, \tag{3.14}$$

and the two-point correlation tensor,

$$R_{ij}(r_\alpha, x_3) = \frac{\langle u_i'(\boldsymbol{x}) u_j'(\boldsymbol{x} + r\hat{\boldsymbol{e}}_\alpha) \rangle}{\langle u_i'^2 \rangle^{1/2} \langle u_j'^2 \rangle^{1/2}}, \tag{3.15}$$

with $\alpha = 1$ and 2. Initially, the peak wavenumbers and the magnitudes of the spectra are all different for the two fluctuating velocity fields (as indicated by the thin curves) throughout the entire depth from the free surface. Nevertheless, as time progresses (thick curves), the two spectra become closer for the whole range of wavenumbers. It is evident that the results demonstrate the convergence of the energy distributions in the fluctuating velocities with different initial conditions from the submerged to the shallow regions of the flow field. This also indicates that the simulated flow reorganizes and, in so doing, eliminates the unphysical nature of the initial random velocity field.

In addition to the above verification regarding the decay of artifacts in generating the flow field, whether or not the flow initialized in such manner eventually becomes representative of turbulence is examined here. Since the Navier–Stokes equation and the kinematic condition of the free-surface elevation (2.3) have been integrated, the validity of the simulated flow can be confirmed by exploring if the processes of energy transfer and dissipation within the underlying turbulence and the interactions among free-surface waves will eventually reach equilibrium status. This is demonstrated by showing the time evolution of the turbulent energy spectra $\mathscr{E}(k, x_3)$ at two depths as

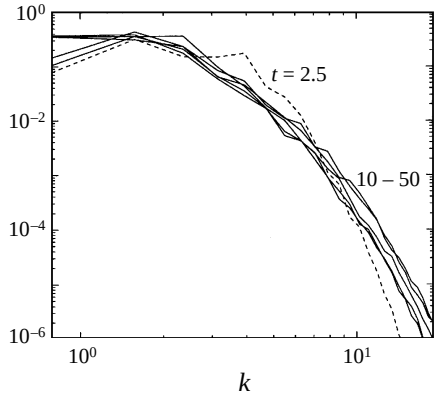

FIGURE 6. Evolution of the one-dimensional free-surface potential energy spectra.

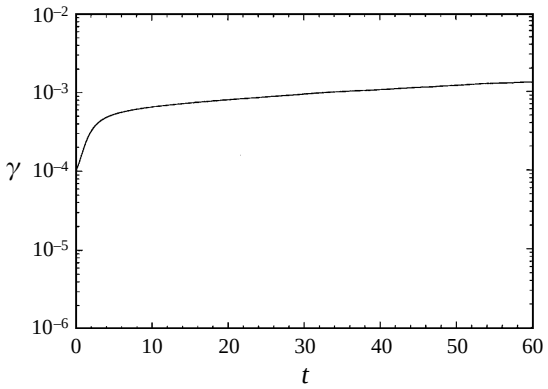

FIGURE 7. Evolution of the relative error of energy conservation $\gamma(t)$.

shown in figure 5. After $t = 20$, the equilibrium range of the energy spectra reaches a convergent distribution for both shallow and submerged depths, though the energy spectra of the short-wavenumber motions continue to evolve. The potential energy spectra of the free-surface deformation also reach equilibrium status quickly after $t = 10$ (figure 6). Hence, it is concluded that as the integration of the momentum equations proceeds, the simulated flow field adjusts itself from an initial artificial random velocity field to realistic turbulence. The growth of the free-surface waves generated by the underlying turbulence and the weakly nonlinear interactions among the waves also reach a state of equilibrium.

In that there are no experimental data available to validate the simulation results, the accuracy of the numerical data is controlled by monitoring the properties of conservation principles, and also by comparing the qualitative properties near the free surface with other open-channel flow simulation results (see §4.1). At the end of the simulation, the mean free surface is conserved to be within $\langle \eta \rangle < 10^{-14}$, while the maximal velocity divergence $u_{i,i}$ is less than 10^{-12}. In order to monitor energy conservation, (2.8) is integrated in time with the simulation. The evolution of the relative error of the energy conservation, $\gamma(t) \equiv |E_k(t) - E_\eta(t) - E_\sigma(t) - E_v(t)|_0^t / E_k(0)$, is plotted in figure 7. After $t \approx 10$, the rate of relative energy lost due to numerical dissipation and errors becomes steady and approaches about 10^{-3}. At the end of the simulation, the energy lost is within 0.1% of the initial total energy. Energy

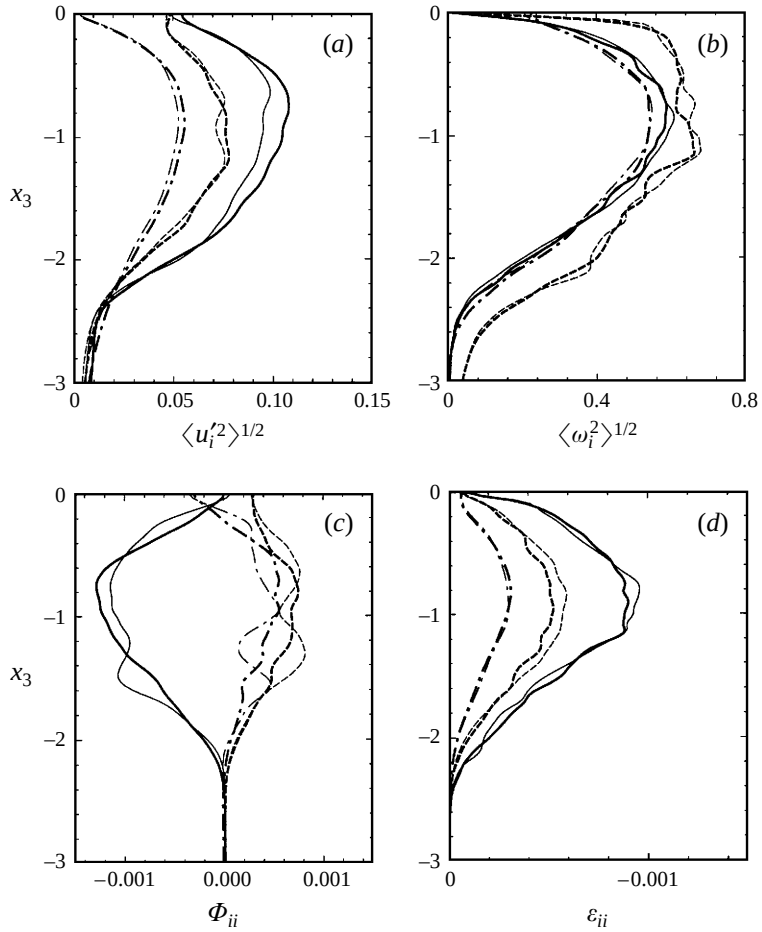

FIGURE 8. Vertical distributions of statistics from two independent simulations (thick and thin lines) at $t = 20$. (*a*) Root-mean-square average of the fluctuating velocity $\langle u_i'^2 \rangle$ of streamwise (———), spanwise (- - - - -) and vertical (— · — · —) components. (*b*) Root-mean-square average of the vorticity $\langle \omega_i^2 \rangle$ of streamwise (———), spanwise (- - - - -) and vertical (— · — · —) components. (*c*) Pressure–strain turbulence production term Φ_{11} (———), Φ_{22} (- - - - -) and Φ_{33} (— · — · —). (*d*) Turbulence dissipation term ε_{11} (———), ε_{22} (- - - - -) and ε_{33} (— · — · —).

conservation is another indicator of the nature of the flow simulated and the state of equilibrium in the dynamic processes of the flow. The error in the energy conservation increases rapidly in the initial stage of the simulation ($t < 10$). Such rapid loss of total energy may be attributed to the initial adjustment of the flow field and the decay in the imposed artifacts (figures 2 to 4). As equilibrium in the inter-scale energy transfer is established (figure 5), energy conservation in the flow simulation should also be reached.

4. Simulation results

For a non-stationary turbulent flow, the convergence of the turbulence statistics is an issue which needs to be verified. To obtain 'good' statistics in numerical simulations of interaction of initially homogeneous turbulence with a free-slip flat surface, Walker

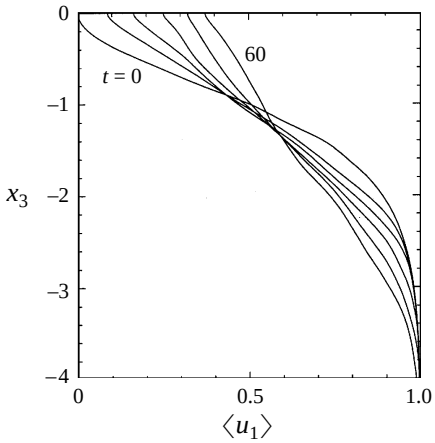

FIGURE 9. Vertical distributions of the streamwise mean velocity $\langle u_1 \rangle$ from $t = 0$ to 60.

et al. (1996) used short-time averaging and exploitation of the reflection and rotation symmetries of the flow, whereas Perot & Moin (1995) performed independent computations (4 to 204 realizations depending on the Reynolds numbers). For the present high-resolution (128^3 grids) simulation, a large number of realizations is restricted by the available computation resources, and most of the turbulence statistics discussed below are from one realization.

To investigate the convergence of the turbulence statistics from the present numerical simulations, two statistically independent computations were performed, and the turbulence statistics were compared. Examples of typical turbulence statistics, which will be discussed below, at the same time for the two independent simulations are shown in figure 8. For the vertical distribution of the fluctuating velocity and vorticity intensities ($\langle u_i'^2 \rangle$ and $\langle \omega_i^2 \rangle$) and the viscous term in velocity fluctuation production ($-2\langle u'_{i,k} u'_{i,k} \rangle / Re$, see §4.1), differences between the two independent realizations are quite smooth. Oscillatory differences are observed in the pressure–strain correlation term ($2\langle p' u'_{i,i} \rangle$, see §4.1) in the submerged region. The distributions of statistics near the free surface, which are of interest in the present study, however, are reasonably convergent, and the two results are qualitatively identical for the flow features discussed below. This indicates that turbulence statistics are indeed representative, and the conclusions drawn from these statistics in the following sections are not affected by the number of realizations.

The simulation was carried out up to $t = 60$. The evolution of the vertical distributions of the streamwise mean velocity $\langle u_1 \rangle$ is shown in figure 9. After $t = 20$, the shear profile of the mean flow becomes linear within the characteristic depth of the shear layer. At the end of the simulation, the mean velocity at the free surface increases to about 0.37. The evolution of turbulence production due to the mean shear of $P_{11} = -\langle u_1' u_3' \rangle \langle u_1 \rangle_{,3}$ is shown in figure 10 for $t = 0$, 30 and 60. The shear production decays for the submerged layer, yet grows for the region near the free surface. This is partially a result of the evolution of the mean flow from the initial hyperbolic profile with inflection to the later linear profile (figure 9).

4.1. *Turbulence energy near the free surface*

Fluctuating turbulence intensities $\langle u_i'^2 \rangle$ are shown in figure 11 for $t = 0$, 30 and 60. Initially, by construction, the turbulence field is isotropic, and all components of the

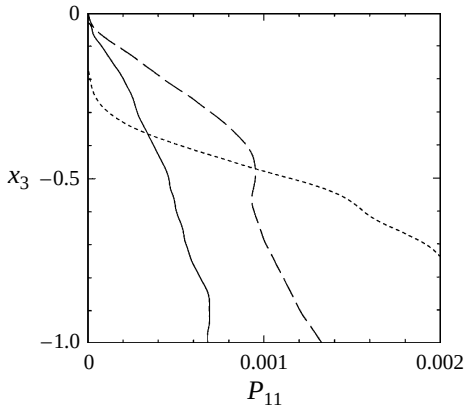

FIGURE 10. Vertical distributions of the turbulence production due to the mean shear P_{11} at $t = 0$ (- - - - -), 30 (— — —) and 60 (———).

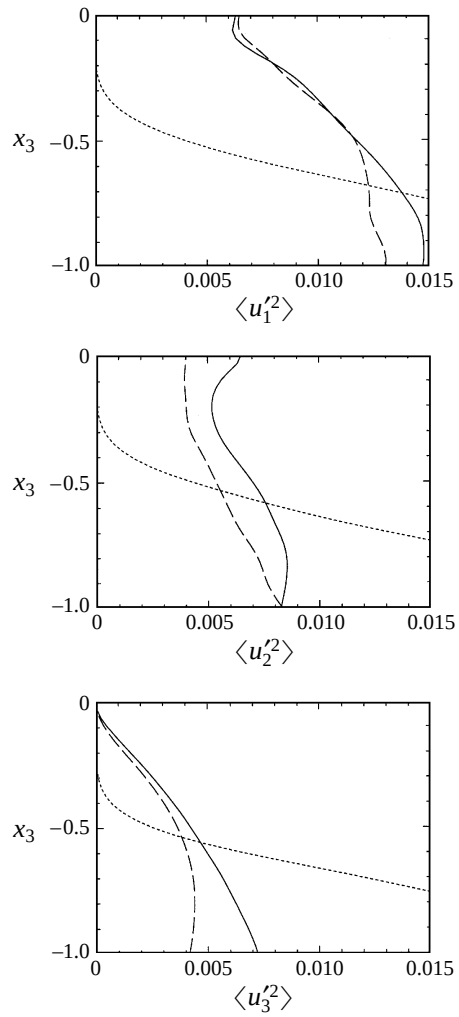

FIGURE 11. Vertical distributions of the variance of the fluctuating velocity $\langle u_i'^2 \rangle$ at $t = 0$ (- - - - -), 30 (— — —) and 60 (———).

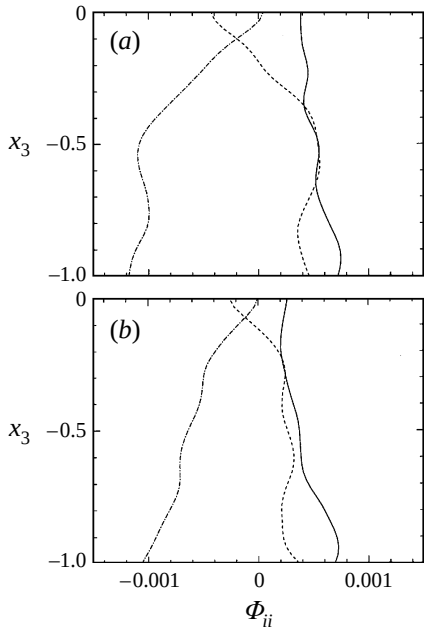

FIGURE 12. Vertical distributions of the pressure–strain turbulence production term Φ_{11} (— · — · —), Φ_{22} (———) and Φ_{33} (- - - - -) at $t = 30$ (*a*) and 60 (*b*).

turbulence intensities approach zero at the free surface. At later times ($t = 30$ and 60), the turbulence field near the free surface becomes effectively anisotropic and two-dimensional, with a rapid attenuation of the vertical fluctuating velocities and an accompanying increase in the horizontal turbulence intensities. The transfer of the turbulence intensity to the spanwise component is more significant than to the streamwise component near the free surface. The same observations were made by Komori *et al.* (1982) and confirmed by Rashidi & Banerjee (1988) in experimental measurements as well as by Lam & Banerjee (1992), Komori *et al.* (1993) and Handler *et al.* (1993) from the numerical simulation results of open-channel flow.

The anisotropic behaviour of the near-surface turbulence was accounted for by Komori *et al.* (1993) and Handler *et al.* (1993) by the considerably greater pressure–strain production of spanwise than streamwise turbulence. The vertical distributions of the pressure–strain turbulence production term $\Phi_{ii} = 2\langle p' u'_{i,i} \rangle$ near the free surface of the present simulation results are shown in figure 12 at $t = 30$ and 60. The variations are qualitatively similar to the simulation results of the open-channel flow by Komori *et al.* (1993) and Handler *et al.* (1993). For the vertical turbulence, the pressure–strain term Φ_{33} changes from production (> 0) to consumption (< 0) at $x_3 \approx 0.2$ when approaching the free surface. This vertical position corresponds to the thickness of the source layer ($\approx$ integral lengthscale of the free-stream turbulence) which is also estimated at 0.2 from figure 11. The Φ_{11} term is negative throughout most of the depth but continues to increase as it approaches the free surface, where it becomes positive. In comparison to Φ_{11}, the spanwise pressure–strain term Φ_{22} is positive throughout the depth. This explains the fact that the blocking effect of the free surface is more significant to the spanwise than to the streamwise turbulence as shown in figure 11.

Anisotropy in turbulence intensities near a free-slip boundary in the absence of

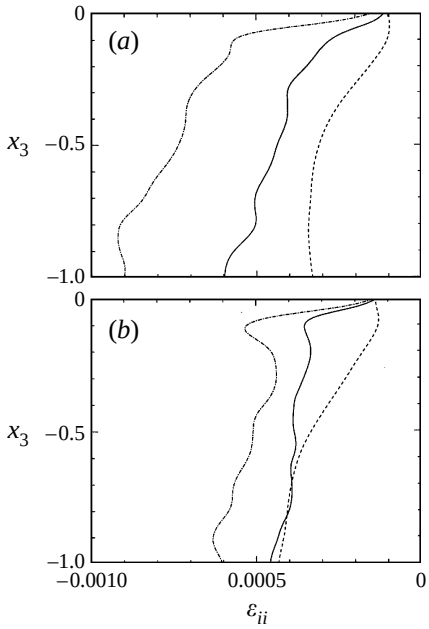

FIGURE 13. Vertical distributions of the turbulence dissipation term ε_{11} (— · — · —), ε_{22} (———) and ε_{33} (- - - - -) at $t = 30$ (*a*) and 60 (*b*).

mean shear was also observed in the numerical studies of the evolution of initial homogeneous and isotropic turbulence by Perot & Moin (1995) and Walker *et al.* (1996). (Perot & Moin also studied the interaction of turbulence with an idealized permeable wall and a no-slip solid wall.) Perot & Moin discussed such anisotropy near the surface in terms of the imbalance between the 'splatting' (upwelling) and 'anti-splatting' (downwelling) structures, which transfers energy from the vertical to horizontal component and vice versa near the boundary. They postulated that such an imbalance is mainly set by viscous effects, and the degree of anisotropy near the free-slip boundary is maintained by reduced dissipation for the horizontal velocity fluctuations. In a similar simulation to Perot & Moin's but over a longer time period, Walker *et al.* (1996) confirmed the conjecture of Perot & Moin. In addition, Walker *et al.* asserted that the reduction in the pressure–strain transfer from the horizontal to vertical velocity fluctuations caused by the boundary and the rapid decay rate of the vertical component caused by dissipation also contribute to the degree of anisotropy near the boundary.

The present simulation (and also those simulations of open-channel flow) differs from the studies of Perot & Moin (1995) and Walker *et al.* (1996) in that mean shear exists in the present turbulent flow. The scenario proposed by Perot & Moin and Walker *et al.*, however, is still applicable to the present flow since turbulence production due to mean shear reduces to a very low level near the free surface (figure 10). To examine the role of viscous dissipation in the redistribution of near-surface turbulence energy, the vertical distributions of the turbulence dissipation rate $\varepsilon_{ii} = -2\langle u'_{i,k} u'_{i,k} \rangle / Re$ at $t = 30$ and 60 are shown in figure 13. The rates of dissipation for the horizontal (streamwise and spanwise) velocity fluctuations decrease drastically on approaching the free surface. (At $t = 60$, the horizontal dissipation rates reach their maxima before reducing to their minima at the free surface. Such a local maximum

rate in the horizontal dissipation is due to large velocity–strain rates caused by the dominant vortex stretching of impinging coherent vortices near the free surface as discussed in §4.4.) The dissipation rate of the vertical velocity fluctuation also reduces, but then increases slightly and reaches a finite level at the free surface, though the vertical velocity fluctuation itself reduces to a very small value. The dissipation rates of horizontal and vertical fluctuations are comparable at the free surface. The consequence is the relatively larger decay rate for the vertical velocity fluctuation than for the horizontal components. These findings are consistent with the results of Perot & Moin and Walker *et al.* for the interaction of initially homogeneous and isotropic turbulence with a free-slip flat surface. In the energy-balance results of Perot & Moin and Walker *et al.*, pressure–strain redistribution was shown to be insignificant in the interaction of horizontally homogeneous turbulence and the free surface. In contrast, in the present turbulent shear flow, both pressure–strain and dissipation terms appear to be the dominant turbulence transfer terms (see figures 12 and 13). The simulation results of Handler *et al.* (1993) for an open-channel flow reveal the same energy balance features near the free surface as those in the present results. This suggests that anisotropic velocity fluctuations of the sheared turbulence beneath a free surface can be attributed to both the effects of pressure–strain correlation and the normalization of the tangential intensity by its free-stream value (as stated in Perot & Moin 1995).

4.2. *Integral lengthscale near the free surface*

The two-point correlation tensor (3.15) is not expected to vanish as $r_\alpha \to \pm\infty$ since the length of the computational domain corresponds to the wavelength of the most unstable mode of the given shear layer. This renders meaningless the definition of the vertical distribution of the integral lengthscale,

$$\Lambda_{ij;\alpha}(x_3) = \int_0^\infty R_{ij}(r_\alpha, x_3)\mathrm{d}r_\alpha. \tag{4.1}$$

Accordingly, the vertical distribution of the integral lengthscale is estimated here by the empirical expression

$$l_i(x_3) = A\frac{\langle (u_i')^2\rangle^{3/2}}{\langle (u_{i,1}')^2\rangle} \tag{4.2}$$

(see e.g. Veeravalli & Warhaft 1989), where $A \equiv Re\,/6$. The vertical variations of the integral lengthscale, l_i/A, at $t = 20$, 30, 40 and 60 are shown in figure 14. Owing to the fact that the vertical turbulence component decays when approaching the free surface, l_3 also reduces to its smallest value on the free surface. The spanwise integral lengthscale, l_2, decreases first from its maximum at the depth of around the thickness of the shear layer but then increases near the free surface and reaches another maximum at the free surface. This also reveals the blocking effect of the free surface discussed previously. The streamwise integral lengthscale, l_1, is much larger than l_2 and l_3 owing to the evolution of the two-dimensional unstable modes of the shear flow. It, however, decreases to a finite value comparable to that of l_2. This is also revealed in the turbulence velocity variances (figure 11).

To further examine the vertical variations of the lengthscales, the one-dimensional energy spectra at three depths, $x_3 \approx -0.031$, -0.281 and -0.719, are plotted in figure 15 for $t = 30$ and 50. For the high-wavenumber range, the slopes of the energy spectra are nearly identical at the different depths thereby indicating that the small-scale turbulence features and energy transport of the flow are similar for the whole

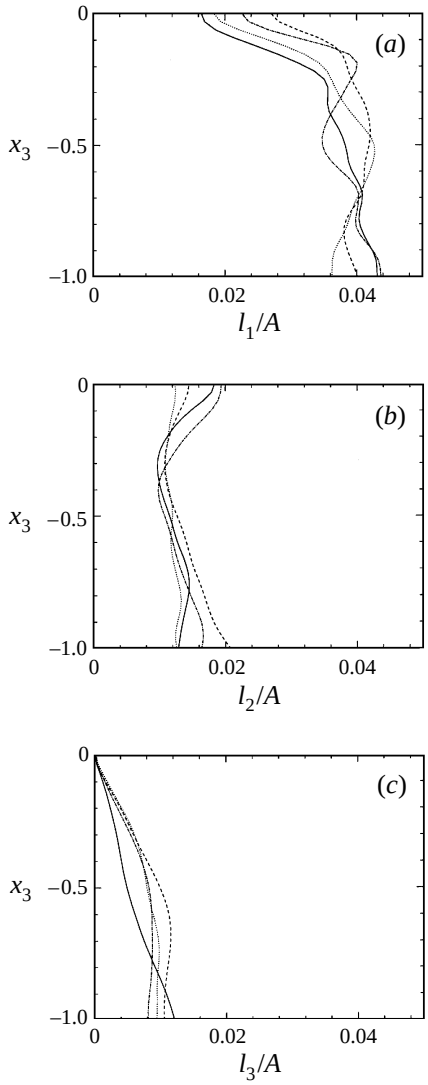

FIGURE 14. Vertical distributions of the integral lengthscale l_i/A at $t = 20$ (- - - - -), 30 (— — —), 40 (— · — · —) and 60 (———).

depth. For the low-wavenumber mode, however, the energy of the large-scale mode grows as it approaches the free surface. The origin of this change in the energy spectrum for different depths is still not clear. It may be due to the backscatter of kinetic energy from the high- to low-wavenumber modes when turbulence approaches the free surface. However, spatial changes in the dissipation spectrum, or possibly variations in the diffusive transport for different wavenumber components, can also lead to such a shift.

4.3. *Vorticity field near the free surface*

The statistical features of the near-surface vorticity field are now focused upon. The variances of the vorticity, $\langle \omega_i^2 \rangle$, are shown in figure 16 for $t = 5$, 30 and 60. In the initial stage, by construction, all of the vorticity variances become negligible near the

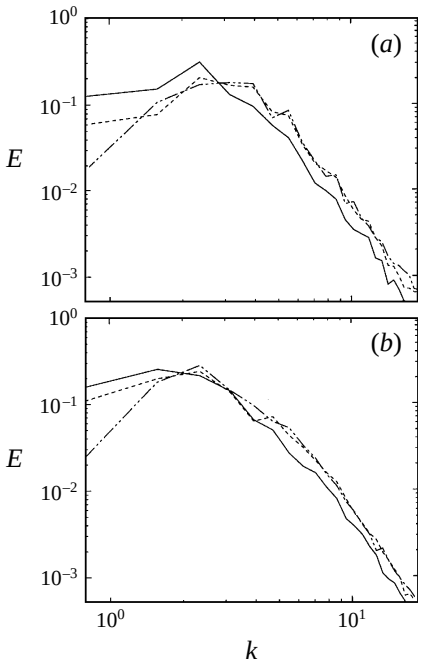

FIGURE 15. One-dimensional energy spectra at $x_3 \approx -0.031$ (———), -0.281 (- - - - -) and -0.719 (— ·· — ·· —), for $t = 30$ (*a*) and 50 (*b*).

free surface. As the underlying turbulent shear flow develops and begins to interact with the free surface, both streamwise- and spanwise-vorticity variances decrease towards the free surface. At the free surface, the streamwise vorticity decreases to a negligible value, whereas the vertical component remains finite. The variance of the spanwise vorticity, nevertheless, reaches its maximum near the free surface but then drops to a negligible value on the free surface. This rise in the spanwise vorticity near the free surface, as a result of vorticity stretching caused by the blocking effect of the free surface on the approaching coherent vortices, is explained in §4.6.

The time evolution of the normal vorticity variance $\langle \omega_3^2 \rangle$ and the horizontal vorticity variance $\langle \omega_1^2 + \omega_2^2 \rangle$ on the mean free surface is shown in figure 17. The variance of the vertical vorticity is much larger than that of the horizontal component throughout the whole simulation time. The difference in the magnitude of the free-surface vorticity component can be explained from the boundary conditions on the free surface. With the perturbation expansions carried out about $x_3 = 0$ and the free-surface dynamic conditions (2.5) and (2.6) applied, the vorticity components on the mean free surface are

$$\omega_1 = 2(u_{3,2})_{x_3=0} + O(\epsilon), \tag{4.3}$$

$$\omega_2 = -2(u_{3,1})_{x_3=0} + O(\epsilon), \tag{4.4}$$

$$\omega_3 = (u_{2,1} - u_{1,2})_{x_3=0} + O(\epsilon/\delta). \tag{4.5}$$

The leading terms of the horizontal vorticities ω_1 and ω_2 are of $O(\delta)$, both of which are much smaller than that of the vertical vorticity ($\sim O(1)$).

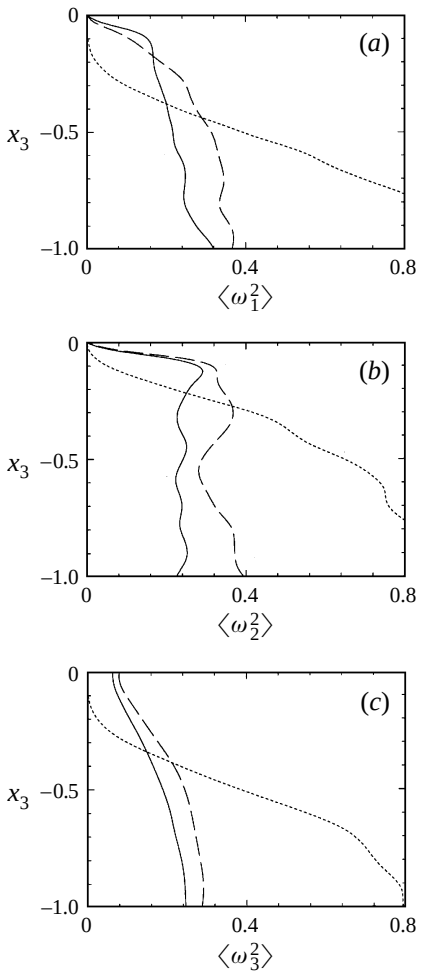

FIGURE 16. Vertical distributions of the variance of the vorticity $\langle\omega_i{}^2\rangle$ at $t = 5$ (- - - - -), 30 (— — —) and 60 (———).

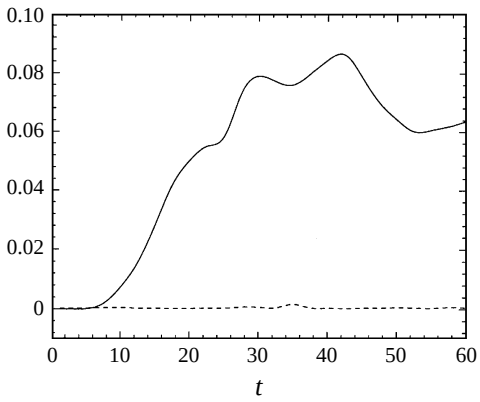

FIGURE 17. Evolution of the normal vorticity variance $\langle\omega_3^2\rangle$ (———) and the horizontal vorticity variance $\langle\omega_1^2 + \omega_2^2\rangle$ (- - - - -) on the mean free surface.

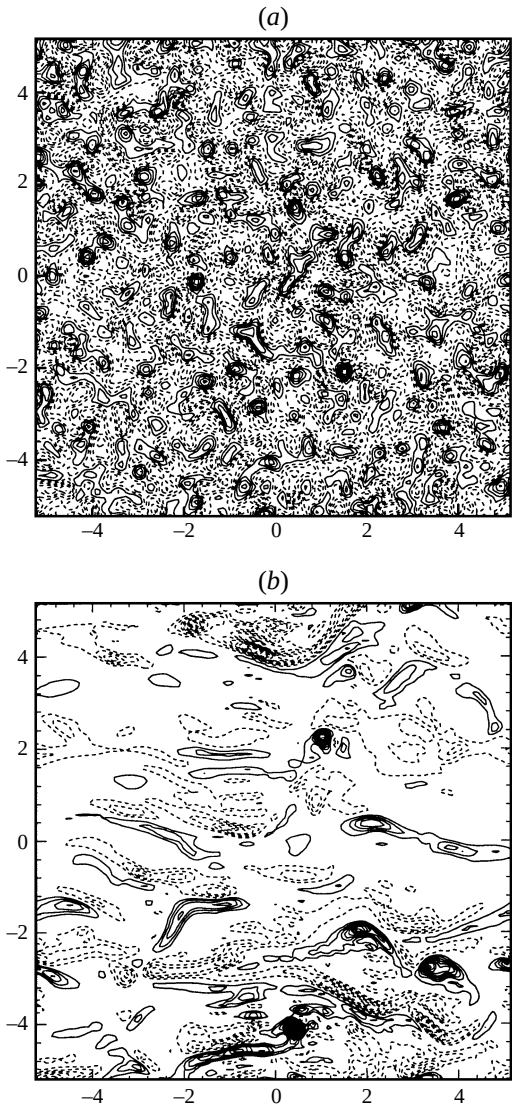

FIGURE 18. Contours of the vertical vorticity ω_3 on the mean free surface at $t = 0$ (*a*) and 32.5 (*b*). 21 contour levels are shown from $\omega_3 = -0.003$ to 0.003 for $t = 0$, and from $\omega_3 = -2$ to 2 for $t = 32.5$. The solid and dashed curves represent positive and negative ω_3 values, respectively.

4.4. *Free-surface signatures*

Accompanying the anisotropic turbulence features near the free surface are vortices with dominant vertical components, ω_3, which emerge on the free surface from random initial vorticities throughout the evolution. Figure 18 shows the vorticity contours on the free surface at $t = 0$ and 32.5. The initial turbulent field has been constructed here such that the normal vorticities have small values and are isotropic, lacking any prescribed structures. As the turbulent flow evolves, dramatic signatures of counter-rotating surface-normal vortices appear on the free surface. Examples of prominent counter-rotating vortex pairs at $t = 32.5$ are located near $(x_1, x_2^+/x_2^-) = (2, -2/-4)$, $(3.6, -4/-2.8)$ and $(0.4, -4/4)$, where x_2^+/x_2^- represents the x_2 coordinate of the

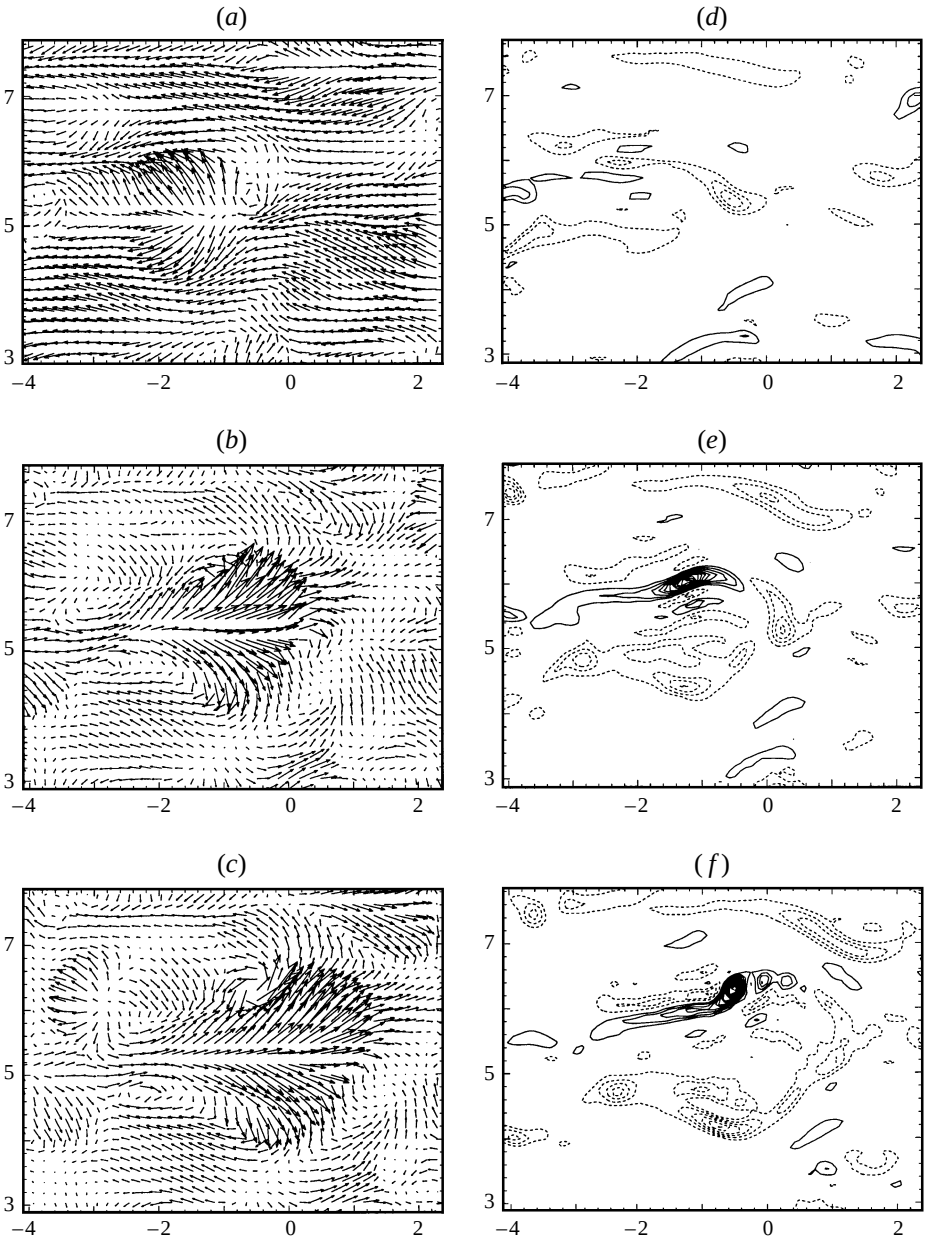

FIGURE 19. Snapshots of the velocity vectors and the vertical vorticity contours on the free surface at $t = 25$ (a, d), 27.5 (b, c) and 30 (c, f), showing the emergence of the counter-rotating vortex pair. 21 contour levels are shown from $\omega_3 = -2$ to 5.

positive/negative vortex. It should be noted that the $(0.4, -4/4)$ pair actually appears at $(0.4, -4/-6.5)$, since the periodic condition is imposed in the x_2-direction. The emergence and the subsequent evolution of this particular counter-rotating vortex pair are focused upon by showing in figure 19 the normal vorticity ω_3 contours on the mean free surface and the corresponding velocity vectors (u_1, u_2) at successive time intervals ($t = 25$, 27.5 and 30). The velocity vector field at $t = 25$ clearly shows

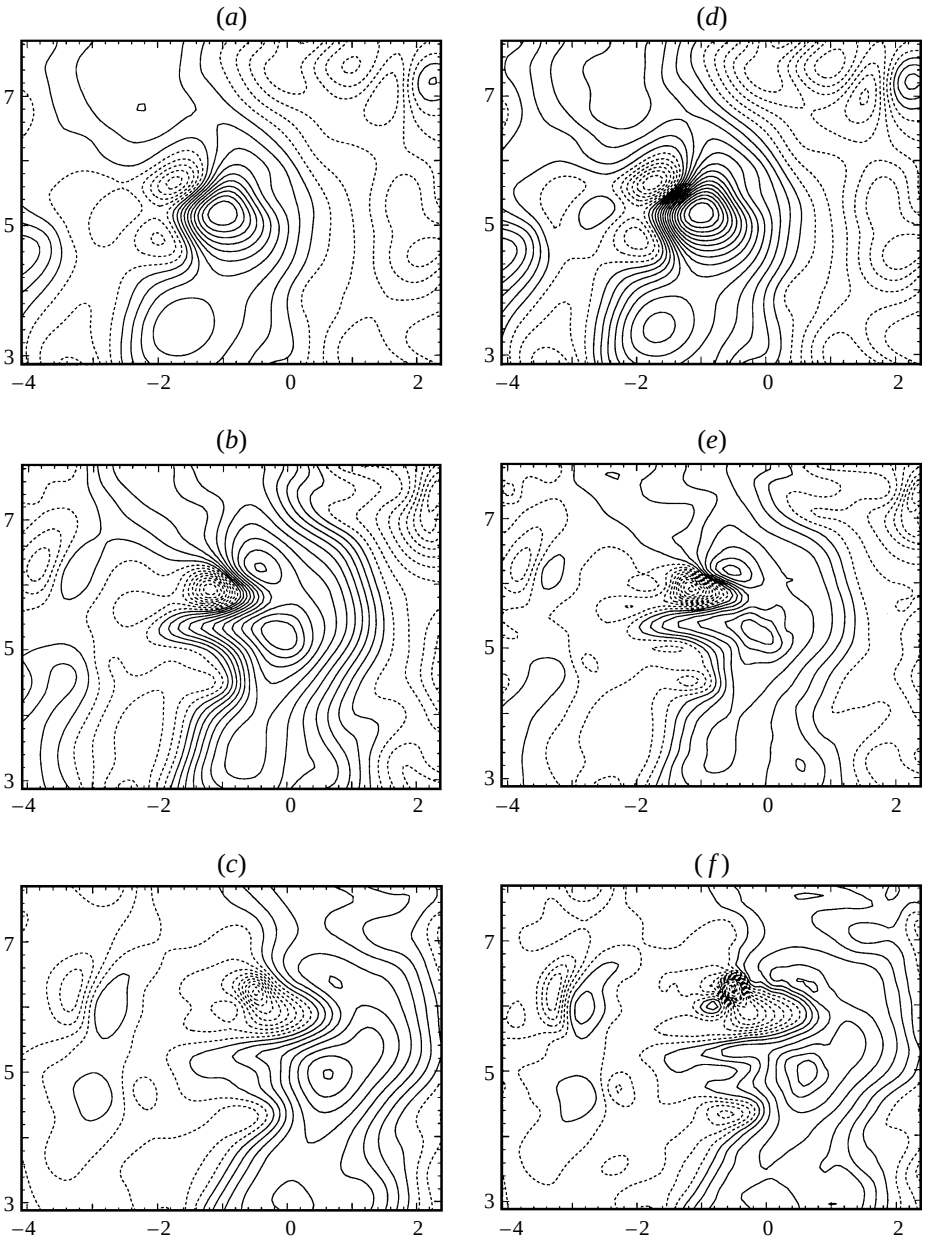

FIGURE 20. Snapshots of the free-surface deformation and the surface pressure contours in the same area as figure 19 at $t = 25$ (a, d), 27.5 (b, c) and 30 (c, f). 21 contour levels are shown from $\eta = -0.02$ to 0.02 and from $p = -0.05$ to 0.05.

an upwelling (splatting) event with a divergent velocity field, which then evolves into a pair of counter-rotating vortices. These vortices appear, grow and then vanish on the free surface, and the whole sequence propagates downstream with the mean flow field. This organized evolution from an upwelling to a counter-rotating vortical flow occurs randomly on the free surface throughout the whole simulation time.

The corresponding sequences of the contours of the free-surface deformation η and

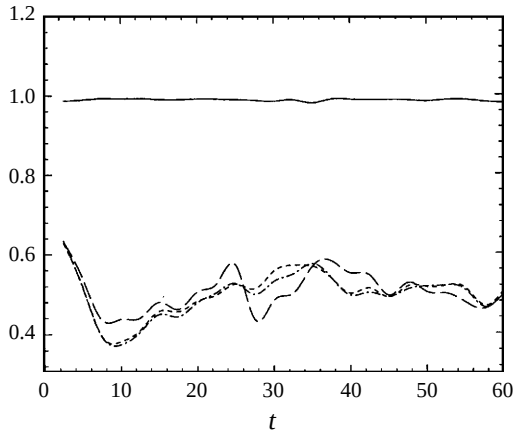

FIGURE 21. Time evolution of the cross-correlation coefficients $C(\eta, p)$ (———), $C(p, \omega_3)$ (— · — · —), $C(\omega_3, \eta)$ (- - - - -) and $C(|\omega_3|, |\eta|; \eta < 0)$ (— — —).

the dynamic pressure p are shown in figure 20. At the stage of upwelling ($t = 25$), the free surface rises and forms a hump near the centre of the velocity divergence. As this hump propagates downstream, two dimples form in the wake of the hump with the centres of the depressions coinciding with those of the counter-rotating vortex pair ($t = 27.5, 30$). The pressure contours are well correlated with the free-surface deformation contours. This is not unexpected in that for a low Froude number flow, the timescale of the vortical motion is larger than that of the free-surface motion, and the pressure on the free surface is mainly balanced by the hydrostatic pressure, i.e. $p \approx \eta/Fr^2$. The normal vorticity centre, the free-surface trough and the low-pressure region occupy the same area on the free surface in the formation of a counter-rotating vorticity connection. This reconfirms the finding that the centre of the coherent structure is a pressure trough (Lesieur, Comte & Métais 1995).

From the experimental or the remote-sensing point of view, it would be desirable to be able to correlate the free-surface roughness with the surface or near-surface flow properties. The cross-correlation coefficients, $C(\eta, p)$, $C(|p|, |\omega_3|)$, $C(|\omega_3|, |\eta|)$ and $C(|\omega_3|, |\eta|; \eta < 0)$, where $C(f, g) \equiv \langle f\, g\rangle/(\langle f^2\rangle^{1/2}\langle g^2\rangle^{1/2})$, are shown in figure 21. The free-surface deformation and pressure have a very strong correlation as predicted. The correlation between the normal vorticity and the free-surface elevation (also the pressure), however, is lower and remains only between 50% and 60% through the whole simulation. Although free-surface dimples form in the same area as the peaks of the vertical-vorticity connections, the correlation between the free-surface depressions and the vertical vorticity, $C(|\omega_3|, |\eta|; \eta < 0)$, is also poor.

To further examine the correlations between the free-surface geometric properties and the tangential vorticities, the kinematic surface condition (2.3) is applied, and the expressions for the streamwise and spanwise surface vorticities (4.4) and (4.5) become

$$\omega_1 \approx 2[\eta_{,t2} + (u_{1,12} + u_{2,22})\eta + u_{1,2}\eta_{,1} + (u_{1,1} + 2u_{2,2})\eta_{,2} + u_1\eta_{,12} + u_2\eta_{,22}], \tag{4.6}$$

$$\omega_2 \approx -2[\eta_{,t1} + (u_{1,22} + u_{2,12})\eta + u_{2,1}\eta_{,2} + (2u_{1,1} + u_{2,2})\eta_{,2} + u_2\eta_{,12} + u_1\eta_{,11}]. \tag{4.7}$$

On the right-hand sides of (4.6) and (4.7), the first terms are associated with the vorticity due to free-surface unsteadiness, while the remaining terms correspond to the free-surface advection effects resulting from the convective terms in the kinematic boundary condition (2.3). In particular, the terms $u_2\eta_{,22}$ and $u_1\eta_{,11}$ are the well-known

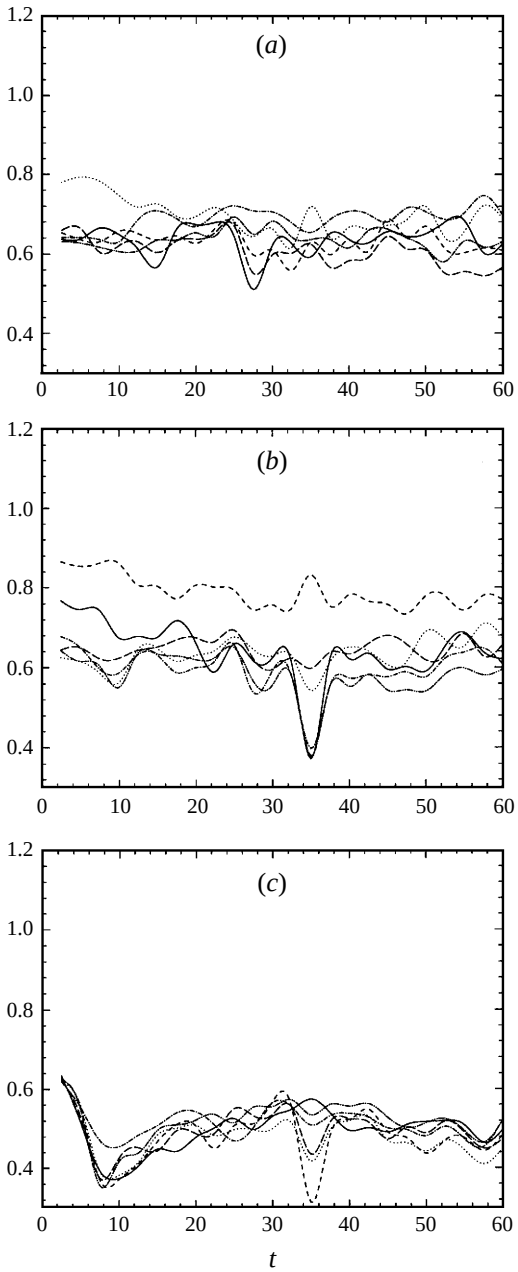

FIGURE 22. Time evolution of the correlation coefficients between the free-surface vorticity (streamwise (*a*), spanwise (*b*) and vertical (*c*)) and the free-surface roughness and its first- and second-order derivatives: $C(\omega_i, \eta)$ (———), $C(\omega_i, \eta_{,11})$ (- - - - -), $C(\omega_i, \eta_{,22})$ (— · — · —), $C(\omega_i, \eta_{,12})$ (· · · · · ·), $C(\omega_i, \eta_{,1})$ (— — —) and $C(\omega_i, \eta_{,2})$ (— ·· — ·· —).

curvature effect (Batchelor 1967). These vorticities vanish when the surface is flat, i.e. the free surface becomes a free-slip boundary. This means that the tangential surface vorticities are mainly attributed to free-surface roughness. The evolution of the correlation coefficients between the free-surface vorticities and the free-surface

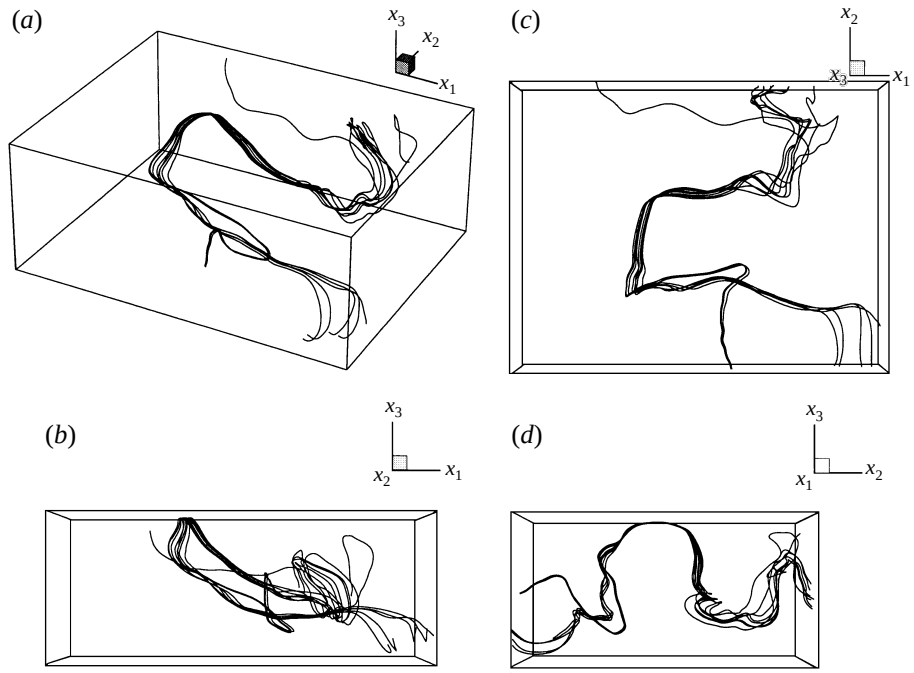

FIGURE 23. Bundle of vortex lines at $t = 25$ displaying the horseshoe-like vortical structure. Perspective (*a*), side (*b*), top (*c*) and front (*d*) views of the vortex lines are shown.

roughness and its first- and second-order derivatives in (4.6) and (4.7) are shown in figure 22. For comparison, the correlations for the vertical vorticity are also presented. The correlations between the surface roughness and its derivatives with the tangential surface vorticities are apparently better than with the normal vorticity. For most of the surface roughness terms, the correlation coefficients for the tangential surface vorticities are between 60% and 70%. The linear curvatures, $\eta_{,11}$ and $\eta_{,22}$, reveal the best correlations of all, especially the $\eta_{,11}$ term of the spanwise vorticity. The correlations between the curvature $\eta_{,11}$ and the spanwise vorticity are between 80% and 90%. This is mainly caused by the convection of the streamwise mean flow and also the impinging spanwise vortical flow, which are discussed later. Such a major induction of the tangential surface vorticity by the free-surface curvatures and the underlying advections was also observed in the two-dimensional interactions of vortical flows with a clean free surface (Tsai & Yue 1995).

4.5. *Underlying coherent vortical structures*

For wall-bounded shear flows, horseshoe (or hairpin) structures in the vorticity field have previously been identified in both experiments and numerical simulations (see e.g. Grass, Stuart & Mansour-Tehrani 1991 and the review by Robinson 1991). Such vortical structures have also been observed in homogeneous turbulent shear flows (e.g. Rogers & Moin 1987). The counter-rotating vorticity connection to the free surface implies that horseshoe vortices formed in the underlying mean shear flow may be responsible for such a dramatic surface feature.

The underlying coherent vortices are sought by tracing vortex lines beginning from normal vorticity maxima on the free surface after the connections appear. The submerged region around the vertical centreplane of the two opposite vortices is then

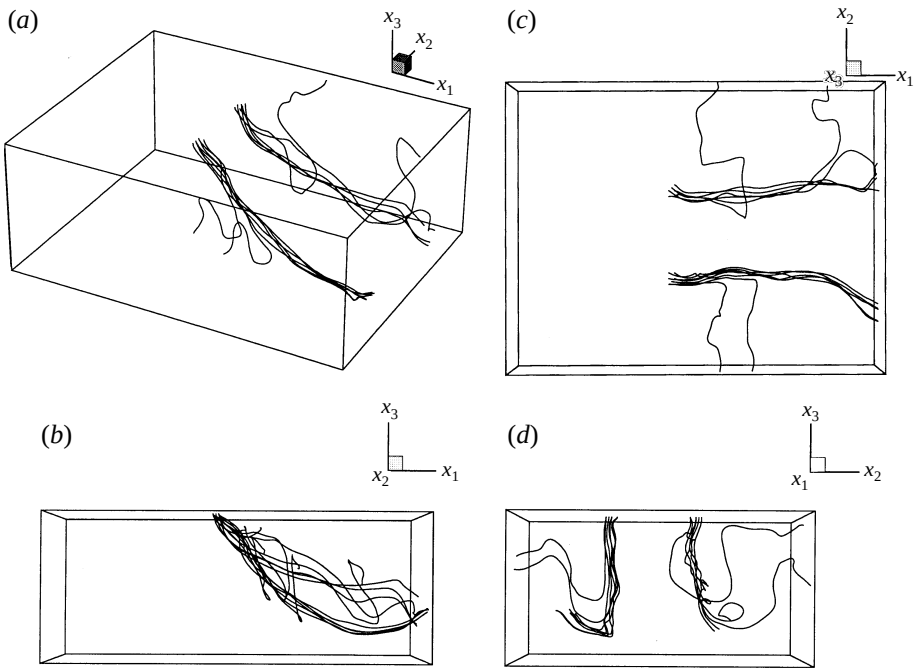

FIGURE 24. Bundle of vortex lines at $t = 27.5$ displaying the connecting vortical structure. Perspective (*a*), side (*b*), top (*c*) and front (*d*) views of the vortex lines are shown.

searched for the vortex lines before the connection. Figures 23 and 24 show typical vortex lines at $t = 25$ and 27.5 (before and after the appearance of the counter-rotating surface vortices). Different perspectives of the vortex lines are shown to illustrate the shapes, orientations and positions of the structures. At $t = 25$, the vortex lines display Ω-shaped horseshoe structures with two elongated legs in the streamwise direction. The direction of vorticity is counterclockwise along the vortex lines moving towards the negative x_2-direction. The two legs extend downstream and downward and then bend outward to form another horseshoe structure with head downward. These vortex lines move upward toward the free surface, and the head of the horseshoe vortex impinges upon the free surface. As the horseshoe vortex continues approaching the free surface ($t = 27.5$ in figure 24), the head of the vortex breaks, and the two shoulders reconnect to the free surface to form two counter-rotating normal vorticies on the surface. The detailed connection processes of the horseshoe vortex to the free surface are discussed in the next subsection.

The definition of a coherent vortical structure has been the subject of vigorous debate. Several eduction techniques have been suggested to identify the coherent structures in a turbulent flow. Examples of these methods include: the use of the isosurfaces of enstrophy $\omega_i\omega_i$ (e.g. Bisset, Antonia & Browne 1990; Hussain & Hayakawa 1987), the eigenvalues of the velocity gradient tensor $u_{i,j}$ (e.g. Chong, Perry & Cantwell 1990), the discriminant of the $u_{i,j}$ tensor (e.g. Blackburn, Mansour & Cantwell 1996), and the eigenvalues of the $S_{i,k}S_{k,j} + \Omega_{i,k}\Omega_{k,j}$ tensor, where $S_{i,j} = (u_{i,j} + u_{j,i})/2$, $\Omega_{i,j} = (u_{i,j} - u_{j,i})/2$ (Jeong & Hussain 1995), among many others. It is still debatable as to which of these methods is the 'best' in identifying coherent vortical structures. To further visualize the three-dimensional vortex structures in figures 23 and 24, in which the traces of vortex lines are used as indicators of the

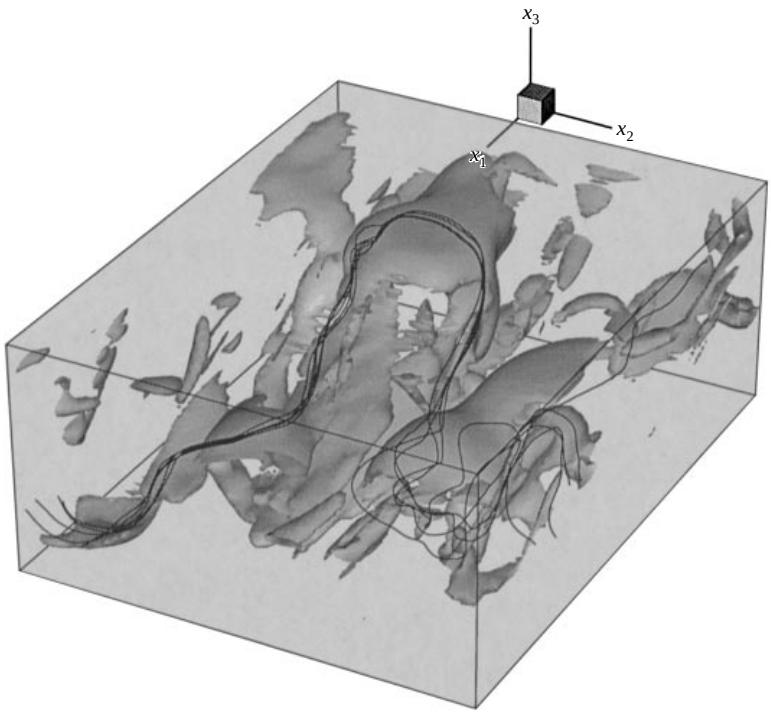

FIGURE 25. Isosurfaces of the enstrophy $\omega_i\omega_i = 1.6$ at $t = 25$ showing the horseshoe vortex structure. The traces of vortex lines are also shown.

structures, isosurfaces of the enstrophy $\omega_i\omega_i$ are shown in figures 25 and 26 for $t = 25$ (horseshoe structure before the connection) and $t = 30$ (after the connection). In order to distinguish the focusing structures in the various isosurfaces, the corresponding vortex lines are also shown. The vortex lines and the isosurfaces display similar shapes and are at the same spatial positions. It should be noted that the vortex lines are traced beginning from the vortex connections on the free surface or the head portion of the vortex near the free surface.

To further confirm the existence of horseshoe vortical structures and the scenario of the vortex connection in the present free-surface turbulent shear flow, the vorticity field is analysed in a manner similar to that in Moin & Kim (1985). The inclination angles of the vorticity vector to the streamwise and spanwise directions: $\theta_i = \tan^{-1}(\omega_3/\omega_i)$, $i = 1, 2$, are calculated at each grid point. The principal values of the angles are defined as $-\pi < \theta_i \leqslant \pi$. Histograms showing the distribution of θ_i at $t = 27.5$ at different depths from the free surface are illustrated in figure 27. The histograms are calculated by sorting θ_i at all the grid points in the horizontal plane with the contribution of each grid point weighted by the normalized magnitude of the projected vorticity vector $(\omega_i^2 + \omega_3^2)/\langle\omega_i^2 + \omega_3^2\rangle$.

In the immediate vicinity of the free surface ($x_3 = -0.0313$ in figure 27*a*), the distribution of θ_1 is highly concentrated around $\pm 90°$, whereas that of θ_2 is around $\pm 90°$ and $\pm 180°$. The vorticity field for such a distribution represents dominant vertical (ω_3) and spanwise (ω_2) vorticities which correspond to the vortex connection onto the free surface and the head portion of the horseshoe vortex. Moving away from the free surface ($x_3 = -0.1$ and -0.5 in figure 27*b*, *c*), the peaks of θ_1 reduce and shift towards $-45°$ and $135°$, indicative of the inclination of the vortex lines

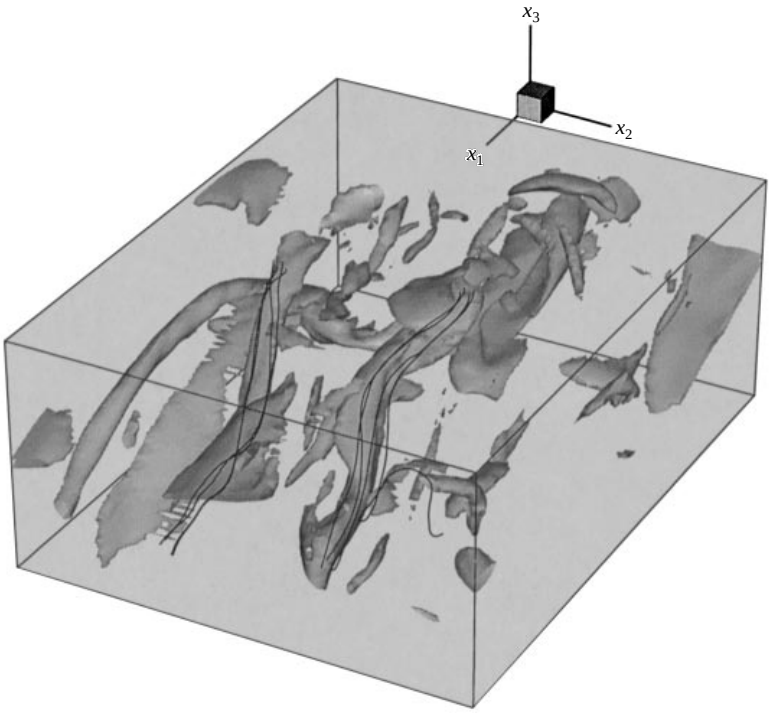

FIGURE 26. Isosurfaces of the enstrophy $\omega_i\omega_i = 1.6$ at $t = 30$ showing the connected vortex structure. The traces of vortex lines are also shown.

with respect to the free stream and consistent with the inclined elongated legs of the structures in figures 23 and 24. The peaks of the θ_2 distribution at $\pm 180^\circ$ away from the free surface are mainly attributed to the spanwise vorticity of the primary two-dimensional shear flow.

4.6. *Free-surface/vortex interaction processes*

For the limiting case of $Fr = 0$, the free surface becomes a free-slip boundary, and the impinging of a vortex onto the surface is identical to the collision of two symmetric vortices with opposite signs. The phenomenon of the breaking and reconnecting of two colliding vortices of various configurations has recently become a topic of considerable research interest. Some examples of numerical simulation of the phenomenon include Melander & Hussain (1989), Kida, Takaoka & Hussain (1991) and Shelley, Meiron & Orszag (1993) among others. Of particular relevance is the reconnection model of Saffman (1990) and its numerical verification by Shelley *et al.* (1993) and it is adopted here to elucidate the dynamics of the breaking and reconnecting to the free surface of the underlying horseshoe vortices. The present study is different from most of these simulations in that the configuration of the vortical flow here is not prescribed but arises from the evolution of a turbulent shear layer.

Figures 28 to 30 present the spanwise vorticity ω_2, the velocity–strain rate $u_{2,2}$ and the vorticity dissipation rate $\omega_{2,ii}/Re$ on the symmetric plane (x_1, x_3-plane) at $t = 20$, 22.5 and 25 of the particular impinging horseshoe vortex and the consequent surface-connected vortex pair discussed in §§4.2 and 4.3. The arrows on the x_1-axis indicate the x_1 positions of the heads of the horseshoe vortices before the connection or the surface vorticity maxima after the connection.

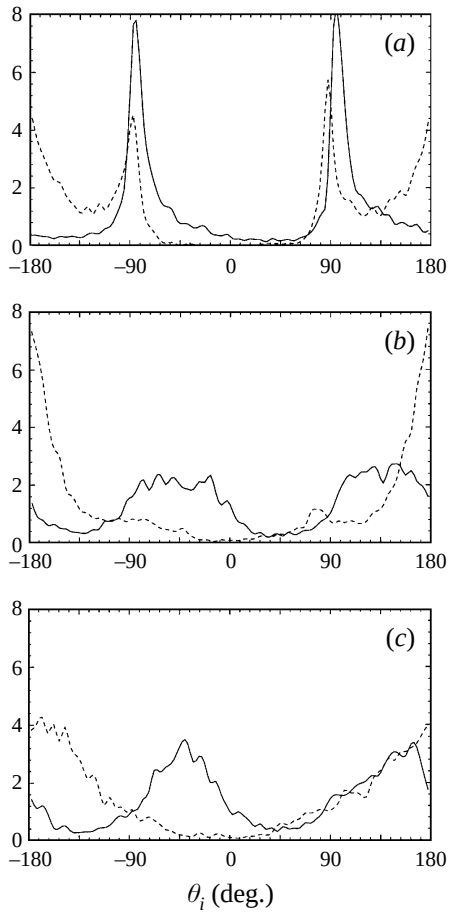

FIGURE 27. Distribution of the inclination angles θ_1 (———) and θ_2 (- - - - -) between the vorticity vectors and the projection of the vectors onto the (x_i, x_3)-planes at $t = 27.5$ for depths $x_3 = -0.0313$ (*a*), -0.1 (*b*) and -0.5 (*c*).

The core of the head of the horseshoe vortex is clearly shown in figure 28 at $t = 20$ and 22.5. As the vortex approaches the free surface, the vorticity core begins to deform and becomes flattened (figure 28*a*, *b*). Meanwhile, the positive spanwise velocity–strain rate, $u_{2,2}$, increases and becomes aligned with the vorticity maximum (figure 29*a*, *b*). This indicates that the head of the horseshoe vortex is stretched spanwise, which leads to an increase in the vorticity strength. Accompanying the increase in the strain rate is the rise in vorticity dissipation due to the viscosity (figure 30*a*, *b*). The distribution of the vorticity dissipation is very localized, being concentrated near the spanwise-vorticity centre. The connection processes, therefore, are determined by the competition between the effects of vortex stretching and dissipation. For the connection to occur, the viscous cancellation of the vorticity continues until it exceeds the stretching effect. Then the dynamics are dominated by the viscous dissipation, and the head of the horseshoe vortex decays (figure 28*c*). The core of the spanwise vortex continues to shrink and the vorticity is annihilated with the approach of the horseshoe vortex towards the free surface. The two shoulders of the horseshoe vortex,

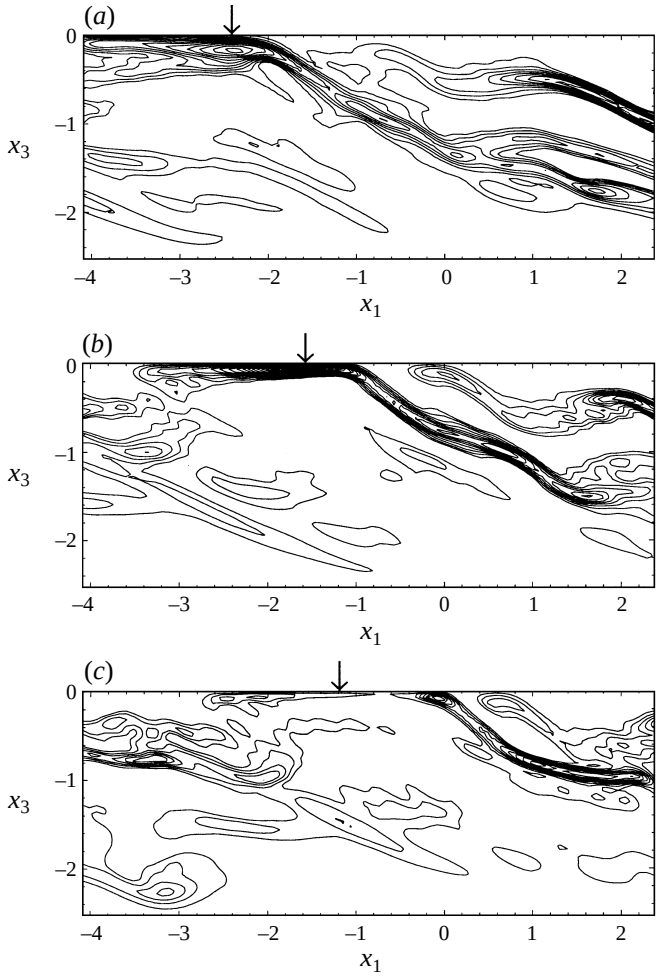

FIGURE 28. Sequences of the spanwise vorticity ω_2 on the symmetric plane (x_1, x_3-plane) at $t = 20$ (*a*), 22.5 (*b*) and 25 (*c*) of the particular impinging horseshoe vortex and the consequent surface-connecting counter-rotating vortex pair shown in figures 23 and 24. 21 contour levels are shown from $\omega_2 = 0$ to 6.

with mainly counter-rotating vertical vorticity, then reconnect onto the free surface and form the counter-rotating vortices on the surface.

So far the disconnection processes of a single horseshoe vortex and its subsequent reconnection to the free surface have been examined. Accordingly, what has been clarified is the issue that the vertically attached vortical structures on the free surface, which have been observed in previous numerous experiments and numerical simulations, may actually originate from approaching surface-parallel vortices, such as the head portion of bursting horseshoe vortices in an open-channel flow. These disconnection and reconnection events are very localized and are solely associated with the coherent vortices. In the following subsection, it is shown that such localized intense events indeed contribute a dominant portion of the fluctuation vorticity dynamics near the free surface. This is done by examining the components in the enstrophy balance and the vorticity transport near the free surface.

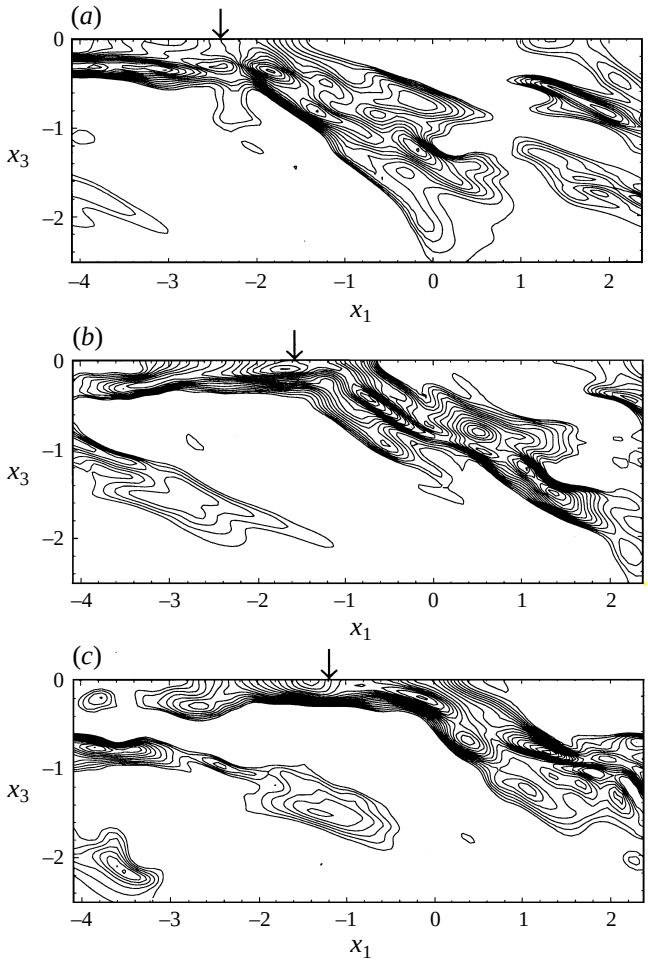

FIGURE 29. Sequences of the velocity–strain rate $u_{2,2}$ on the symmetric plane (x_1, x_3-plane) at $t = 20$ (*a*), 22.5 (*b*) and 25 (*c*) of the particular impinging horseshoe vortex and the consequent surface-connecting counter-rotating vortex pair shown in figures 23 and 24. 21 contour levels are shown from $\omega_2 = 0$ to 1.

4.7. *Enstrophy balance and vorticity transport*

The enstrophy balance equation of the vorticity field is given as

$$\frac{\mathrm{D}\Omega_i}{\mathrm{D}t} = \omega_i \omega_j u_{i,j} + \frac{1}{Re}(\Omega_{i,jj} - \omega_{i,j}\omega_{i,j}), \tag{4.8}$$

where the enstrophy $\Omega_i \equiv \frac{1}{2}\omega_i^2$, and the summation is implied only for the j index. The $\omega_i \omega_j u_{i,j}$ term in (4.8) represents the production of the enstrophy Ω_i due to the stretching or compression of ω_i vorticity when $i = j$, or because of the rotation from ω_j to ω_i when $i \neq j$. The last two terms in (4.8) represent viscous diffusion and dissipation, respectively. The previous observation of the horseshoe vortex connection to the free surface implies that the major spanwise vortex dynamics near the free surface are vortex stretching and viscous dissipation. Figure 31(*a*) presents the vertical variations of the average spanwise enstrophy transport terms $\langle \omega_2 \omega_j u_{2,j} \rangle$ and $\langle \Omega_{2,jj} - \omega_{2,j}^2 \rangle / Re$ at $t = 30$. Approaching the free surface, both the vorticity stretching and dissipation

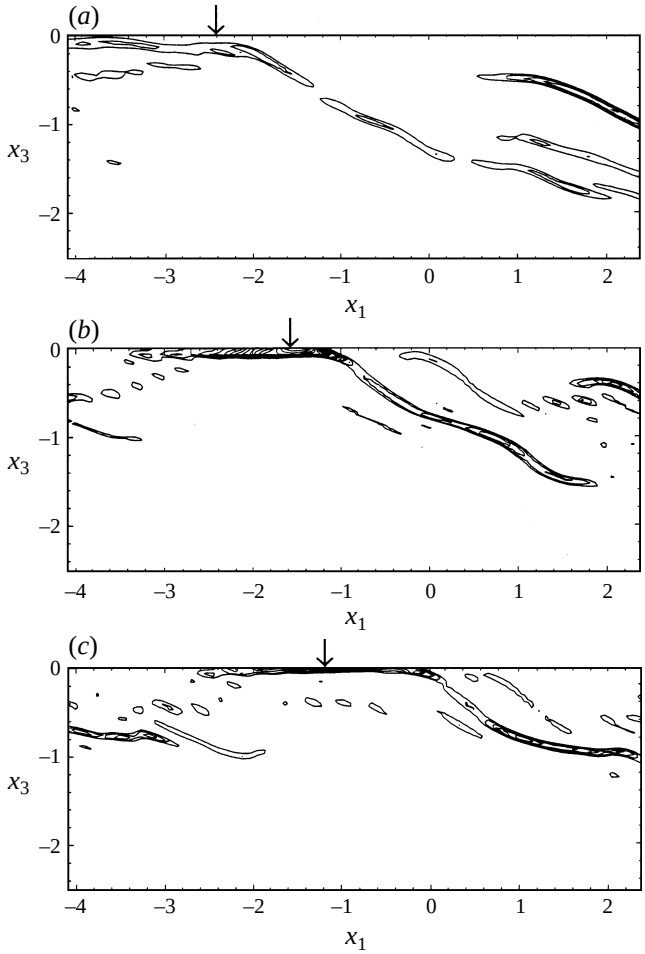

FIGURE 30. Sequences of the vorticity dissipation rate $\omega_{2,ii}/Re$ on the symmetric plane (x_1, x_3-plane) at $t = 20$ (*a*), 22.5 (*b*) and 25 (*c*) of the particular impinging horseshoe vortex and the consequent surface-connecting counter-rotating vortex pair shown in figures 23 and 24. 21 contour levels are shown from $\omega_2 = 0$ to 4.

rates increase to significant magnitudes but with opposite signs, and then decrease to negligible values. Compared to vortex stretching, the vortex rotation from streamwise and vertical to spanwise vorticity is much less significant. This confirms the notion that the production of the normal vorticity on the free surface is induced by the connecting processes discussed above. The vortex rotation events from horizontal to vertical vanish near the free surface.

Once the connecting processes of the vortex to the free surface are complete, the connected counter-rotating vortices move downstream with the mean velocity, and the magnitudes of vorticity increase at first but then decay with the sequences of ω_3 contours shown in figure 19 for $t = 25$, 27.5 and 30 and figure 32 for $t = 30$, 32.5 and 35. In figure 31(*b*) the vertical variations of the average vertical enstrophy transport terms $\langle \omega_3 \omega_j u_{3,j} \rangle$ and $\langle \Omega_{3,jj} - \omega_{3,j}^2 \rangle / Re$ at $t = 30$ are plotted. The dynamics of vertical vortex stretching remain effective up to the free surface, where the vortex rotation vanishes. The viscous vorticity decay rate decreases on approaching the free

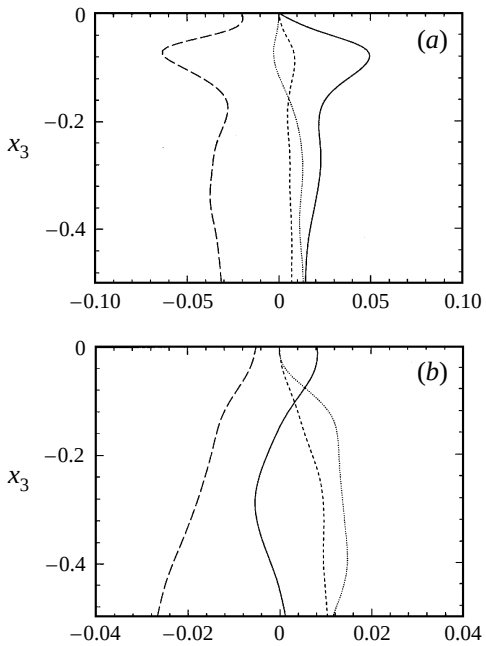

FIGURE 31. Vertical variations of the average (*a*) spanwise enstrophy transport terms $\langle \omega_2^2 u_{2,2} \rangle$ (———), $\langle \omega_2 \omega_1 u_{2,1} \rangle$ (- - - - -), $\langle \omega_2 \omega_3 u_{2,3} \rangle$ (· · · · · ·) and $\langle \Omega_{2,jj} - \omega_{2,j}^2 \rangle / Re$ (— — —); and (*b*) vertical enstrophy transport terms $\langle \omega_3^2 u_{3,3} \rangle$ (———), $\langle \omega_3 \omega_1 u_{2,1} \rangle$ (- - - - -), $\langle \omega_3 \omega_2 u_{2,2} \rangle$ (· · · · · ·) and $\langle \Omega_{3,jj} - \omega_{3,j}^2 \rangle / Re$ (— — —) at $t = 30$.

surface; however, it still remains at a finite value, suggesting that the annihilation of the surface-connected vortex may also be caused by the competition between the vertical vortex stretching and viscous dissipation. The evolution of the surface ω_3 dissipation rate $\langle \Omega_{3,jj} - \omega_{3,j}^2 \rangle / Re$ is also shown in figure 32 with the corresponding ω_3 contours. The regions of maximal viscous dissipation coincide with the surface-connected vortices. This observation indicates that after the reconnection of the broken horseshoe-vortex legs to the free surface, stretching and viscous dissipation are the only mechanisms responsible for the annihilation of the counter-rotating connected surface vortices.

To further elucidate the vortex dynamics of the underlying shear flow, the vorticity transport equation

$$\frac{\mathrm{D}\omega_i}{\mathrm{D}t} = \omega_{i,t} + u_j \omega_{i,j} = \omega_j S_{ij} + \frac{1}{Re} \omega_{i,jj}, \tag{4.9}$$

where $S_{ij} = \frac{1}{2}(u_{i,j} + u_{j,i})$ is the strain-rate tensor, is projected onto the directions tangential and perpendicular to the vorticity vector with $\hat{s} = s_i$ and $\hat{t} = t_i$ as the directional unit vectors. The vorticity transport rate associated with velocity strain can then be decomposed into the stretching (also compressing) rate along the vorticity vector, $\psi_i^s = (\omega_j S_{lj} s_l) s_i$ and the turning rate normal to the vorticity vector, $\psi_i^t = \omega_j S_{ij} - \psi_i^s$. Similarly, the transport rate associated with viscous dissipation can also be decomposed into $\chi_i^s = (\omega_{l,jj} s_l) s_i / Re$ and $\chi_i^t = \omega_{i,jj}/Re - \chi_i^s$, which are tangential and perpendicular to the vorticity vector, respectively.

The vertical distributions of the variance of the vorticity transport rate are shown in figure 33 for $t = 30$ and 60. The distributions are qualitatively similar for the

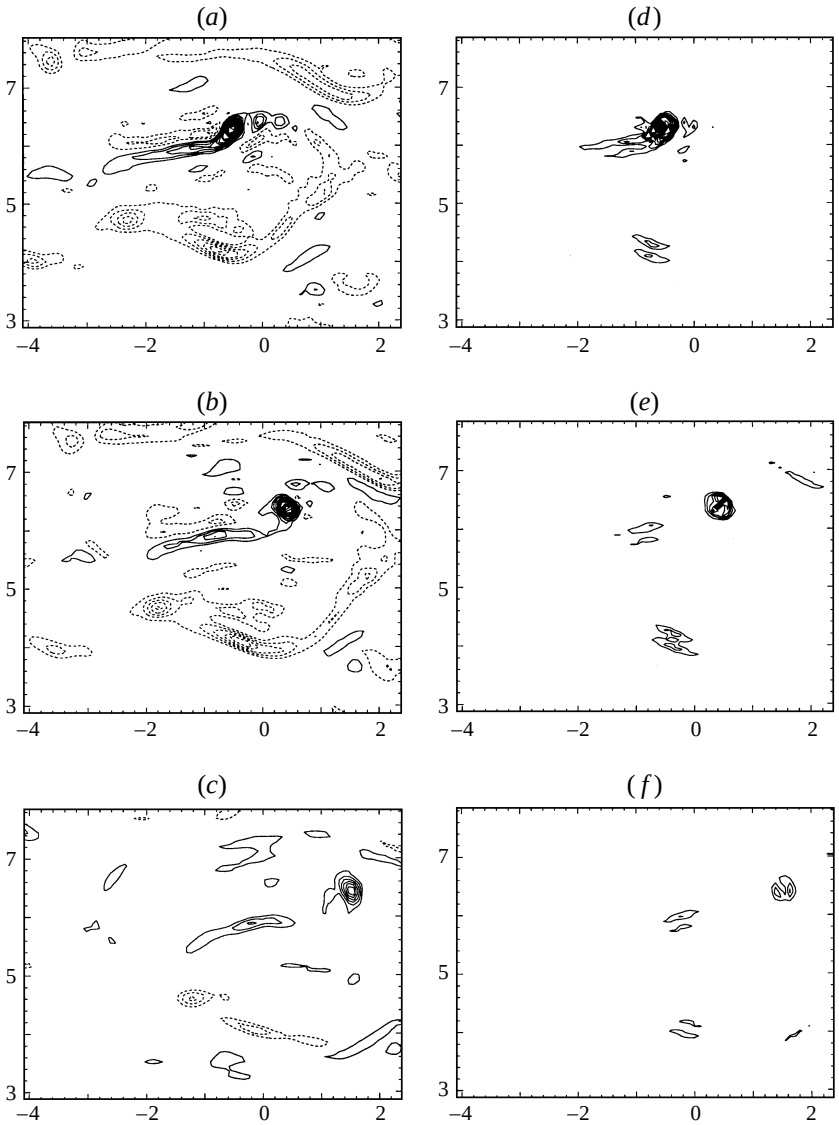

FIGURE 32. Snapshots of the vertical vorticity contours and the average vertical enstrophy dissipation rate on the free surface at $t = 30$ (a, d), 32.5 (b, c) and 35 (c, f), showing the annihilation of the counter-rotating vortex pair. 21 contour levels are shown from $\omega_3 = -2$ to 5 and $\langle \Omega_{3,jj} - \omega_{3,j}^2 \rangle / Re = -2$ to 0.

vorticity fields at $t = 30$ and 60. The vorticity compressing rate ($\psi_i^s < 0$) is negligible throughout the entire depth compared to the vorticity stretching rate ($\psi_i^s > 0$). The vortex turning and stretching rates are comparable for the submerged ($x_3 < -0.2$ approximately) vorticity field. Near the free surface, the turning rate reduces dramatically. The stretching rate, nevertheless, increases to its maximum near the free surface. Slightly above the depth where the stretching rate reaches its maximum, the viscous dissipation rate also increases to a maximum. At this maximal dissipation rate, the dissipation is mainly contributed by the velocity deformation along the vorticity-vector direction, i.e. $\langle (\chi_i^s)^2 \rangle \gg \langle (\chi_i^t)^2 \rangle$. These observations of vorticity transport budget

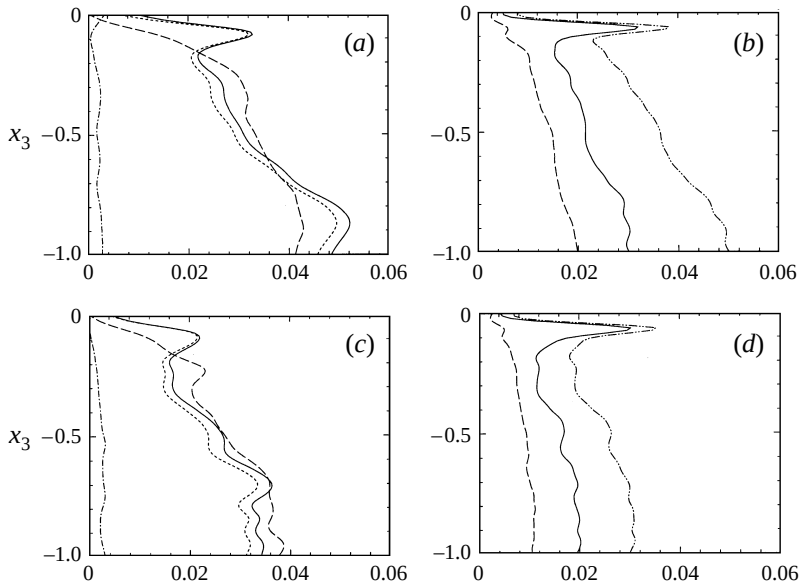

FIGURE 33. Vertical distributions of the variance of vorticity transport rate associated with velocity strain (a, c): $\langle(\psi_i^s)^2\rangle$ (———), $\langle(\psi_i^t)^2\rangle$ (— — —), $\langle(\psi_i^s)^2\rangle$ with $\psi_i^s > 0$ (- - - - -) and $\langle(\psi_i^s)^2\rangle$ with $\psi_i^s < 0$ (— · — · —), and the transport rate associated with viscous dissipation (b, d): $\langle(\chi_i^s + \chi_i^t)^2\rangle$ (— ·· — ·· —), $\langle(\chi_i^s)^2\rangle$ (———) and $\langle(\chi_i^t)^2\rangle$ (— — —), for $t = 30$ (a, b) and 60 (c, d).

confirm the previously discussed scenarios regarding the breaking and reconnection of the horseshoe vortices to the free surface.

Right on the free surface, the turning rate of the vorticity $\langle(\psi_i^t)^2\rangle$ vanishes, and the vortex dynamics are controlled by stretching and dissipation. The dissipation rate along the vorticity vector (vertical) direction is larger than on the horizontal plane ($\langle(\chi_i^s)^2\rangle > \langle(\chi_i^t)^2\rangle$). This, again, supports the mechanism discussed earlier regarding the annihilation of the connected vortices.

5. Concluding remarks

The interactions between a free surface and an underlying shear layer with initially isotropic three-dimensional turbulence are investigated in this paper. Some key findings of the present numerical simulation results are:

(i) Accompanying the quasi-two-dimensionality of the flow field approaching the free surface, the macroscales of the turbulence near the surface increase, and the energy of the low-wavenumber modes appears to increase. Both the pressure–strain correlations and the viscous dissipation in the velocity fluctuations were shown to contribute to the anisotropic distribution of turbulence energy near the free surface.

(ii) Coherent horseshoe vortices, which evolve from the initial horizontally homogeneous turbulent shear flow, impinge upon the free surface, break and reconnect to the surface. During the process of connection, two dimples (depressions) form on the free surface near the maximal connected vorticity centres. The global correlation between the free-surface roughness and the surface normal vorticity, however, is poor. The well-known free-surface curvatures and tangential vorticities, on the other hand, have the best correlations among the other surface roughness and vorticity components.

(iii) Near the free-surface, vortex turning vanishes; instead, stretching as well

as viscous dissipation and diffusion along the vorticity-vector direction dominate the vorticity transport budget. The vortex stretching events are enhanced by the blocking effect of the free surface, which deforms the impinging vortex cores and leads to intensified velocity strain. This results in the continuous growth of the viscous dissipation and diffusion of the stretched vorticity. It also explains the fact that although the stretching mechanism generates small-scale vortices, the dominant viscous effect effectively damps out these short-wavelength modes, and the kinetic energy accumulates in the low-wavenumber modes.

The author is grateful to the anonymous reviewers for their constructive comments which have led to an improved presentation of these results. This research was started while the author was affiliated to the Massachusetts Institute of Technology and has been supported by grants from the Office of Naval Research, though the computations and the major part of the analyses were finished at Taiwan Ocean University and sponsored by the National Science Council of the Republic of China (grants NSC 85-2611-M-019-007 and 86-2611-M-019-002). Supercomputing time was provided by the National Center for High-Performance Computing of Taiwan and the Taiwan Ocean University Computer Center.

REFERENCES

Anthony, D. G. & Willmarth, W. W. 1992 Turbulence measurements in a round jet near a free surface. *J. Fluid Mech.* **243**, 699–720.

Batchelor, G. K. 1967 *An Introduction to Fluid Dynamics*. Cambridge University Press.

Bisset, D. K., Antonia, R. A. & Browne, L. W. B. 1990 Spatial organization of large structures in the turbulent far wake of a cylinder. *J. Fluid Mech.* **218**, 439–461.

Blackburn, H. M., Mansour, N. N. & Cantwell, B. J. 1996 Topology of fine-scale motions in turbulent channel flow. *J. Fluid Mech.* **310**, 269–292.

Borue, V., Orszag, S. A. & Staroselsky, I. 1995 Interaction of surface waves with turbulence: direct numerical simulation of turbulent open-channel flow. *J. Fluid Mech.* **286**, 1–23.

Brumley, B. H. & Jirka, G. H. 1987 Near-surface turbulence in a grid-stirred tank. *J. Fluid Mech.* **183**, 235–263.

Chong, M. S., Perry, A. E. & Cantwell, B. J. 1990 A general classification of three-dimensional flow field. *Phys. Fluids* A **2**, 765–777.

Gharib, M. 1994 Some aspects of near-surface vortices. In *Proc. Twelfth US National Congress of Applied Mechanics, June 1994, Seattle, WA* (ed. A. S. Kobayashi), *Appl. Mech. Rev.* **47**, S157–S163.

Gharib, M. & Weigand, A. 1996 Experimental studies of vortex disconnection and connection at a free surface. *J. Fluid Mech.* **321**, 59–86.

Grass, A. J., Stuart, R. J. & Mansour-Tehrani, M. 1991 Vortical structures and coherent motion in turbulent flow over smooth and rough boundaries. *Phil. Trans. R. Soc. Lond.* A **336**, 35–65.

Handler, R. A., Swean, Jr., T. F., Leighton, R. I. & Swearingen, J. D. 1993 Length scales and the energy balance for turbulence near a free surface. *AIAA J.* **31**, 1998–2007.

Hunt, J. C. R. 1984 Turbulence structure and turbulent diffusion near gas–liquid interfaces. In *Gas Transfer at Water Surfaces* (ed. W. Brutsaert & G. H. Jirka), pp. 67–82. D. Reidel.

Hunt, J. C. R. & Graham, J. M. R. 1978 Free-stream turbulence near plane boundaries. *J. Fluid Mech.* **84**, 209–235.

Hussain, A. K. M. F. & Hayakawa, M. 1987 Eduction of large-scale organized structure in a turbulent plane wake. *J. Fluid Mech.* **180**, 193–229.

Jeong, J. & Hussain, F. 1995 On the identification of a vortex. *J. Fluid Mech.* **285**, 69–94.

Kida, S., Takaoka, M. & Hussain, F. 1991 Collision of two vortex rings. *J. Fluid Mech.* **230**, 583–646.

Komori, S., Murakami, Y. & Ueda, H. 1989 The relationship between surface-renewal and bursting motions in open-channel flow. *J. Fluid Mech.* **203**, 103–123.

Komori, S., Nagaosa, R., Murakami, Y., Chiba, S., Ishii, K. & Kuwahara, K. 1993 Direct numerical simulation of three-dimensional open-channel flow with zero-shear gas-liquid interface. *Phys. Fluids* A **5**, 115–125.

Komori, S., Ueda, H., Ogino, F. & Mizushina, T. 1982 Turbulence structure and transport mechanism at the free surface in an open channel flow. *Intl J. Heat Mass Transfer* **25**, 513–521.

Lam, K. & Banerjee, S. 1992 On the condition of streak formation in a bounded turbulent flow. *Phys. Fluids* A **4**, 306–320.

Leighton, R. I., Swean, Jr., T. F., Handler, R. A. & Swearingen, J. D. 1991 Interaction of vorticity with a free surface in turbulent open channel flow. *AIAA Paper* 91-0236.

Lesieur, M., Comte, P. & Métais, O. 1995 Numerical simulations of coherent vortices in turbulence. *Appl. Mech. Rev.* **48**, 121–149.

Madnia, K. & Bernal, L. P. 1993 Interaction of a turbulent round jet with the free surface. *J. Fluid Mech.* **261**, 305–332.

Mattingly, G. E. & Criminale, W. O. 1972 The stability of an incompressible two-dimensional wake. *J. Fluid Mech.* **51**, 233–272.

Melander, M. V. & Hussain, F. 1989 Cross-linking of two antiparallel vortex tubes. *Phys. Fluids* A **1**, 633–636.

Moin, P. & Kim, J. 1985 The structure of the vorticity field in turbulent channel flow. Part 1. Analysis of instantaneous fields and statistical correlations. *J. Fluid Mech.* **155**, 441–464.

Nezu, I. & Nakagawa, H. 1993 *Turbulence in Open-Channel Flows*. Rotterdam: A. A. Balkema.

Ölmez, H. S. & Milgram, J. H. 1992 An experimental study of attenuation of short water waves by turbulence. *J. Fluid Mech.* **239**, 133–156.

Pan, Y. & Banerjee, S. 1995 A numerical study of free-surface turbulence in channel flow. *Phys. Fluids* **7**, 1649–1664.

Perot, B. & Moin, P. 1995 Shear-free turbulent boundary layers. Part 1. Physical insights into near-wall turbulence. *J. Fluid Mech.* **295**, 199–227.

Rashidi, M. & Banerjee, S. 1988 Turbulence structure in free-surface channel flows. *Phys. Fluids* **31**, 2491–2503.

Robinson, S. K. 1991 Coherent motions in the turbulent boundary layer. *Ann. Rev. Fluid Mech.* **23**, 601–639.

Rogers, M. M. & P. Moin, P. 1987 The structure of the vorticity field in homogeneous turbulent flows. *J. Fluid Mech.* **176**, 33–66.

Saffman, P. G. 1990 A model of vortex reconnection. *J. Fluid Mech.* **212**, 395–402.

Shelley, M. J., Meiron, D. I. & Orszag, S. A. 1993 Dynamical aspects of vortex reconnection of perturbed anti-parallel vortex tubes. *J. Fluid Mech.* **246**, 613–652.

Swean, T. F., Ramberg, S. E., Plesnia, M. W. & Stewart, M. B. 1989 Turbulent surface jet in a channel of limited depth. *J. Hydraul. Engng* **115**, 1587–1606.

Triantafyllou, G. S. & Dimas, A. A. 1989 Interaction of a two-dimensional separated flow with a free surface at low Froude numbers. *Phys. Fluids* A **4**, 1215–1229.

Tsai, W.-T. & Yue, D. K. P. 1995 Effects of soluble and insoluble surfactant on laminar interactions of vortical flows with a free surface. *J. Fluid Mech.* **289**, 315–349.

Tsai, W.-T. & Yue, D. K. P. 1996 Computation of nonlinear free-surface flows. *Ann. Rev. Fluid Mech.* **28**, 249–278.

Veeravalli, S. & Warhaft, Z. 1989 The shearless turbulence mixing layer. *J. Fluid Mech.* **207**, 191–229.

Walker, D. T., Chen, C.-Y. & Willmarth, W. W. 1995 Turbulent structure in free-surface jet flows. *J. Fluid Mech.* **291**, 223–261.

Walker, D. T., Leighton, R. I. & Garza-Rios, L. O. 1996 Shear-free turbulence near a flat free surface. *J. Fluid Mech.* **320**, 19–51.

Wu, J. 1975 Wind-induced drift currents. *J. Fluid Mech.* **68**, 49–70.

Wu, J. 1983 Sea-surface drift currents induced by wind and waves. *J. Phys. Oceanogr.* **13**, 1441–1451.